Fatigue Properties of Tungsten Heavy Alloys IT180 and D176

AUTHORS: Marc Miralda López, Patricia Lorenzo Paez

SUPERVISORS: Srinivasan Iyengar, Lund University
                Etam Noah, European Spallation Source (ESS),Lund

EXAMINER: Solveig Melin, Lund University

To our parents

Abstract

Fatigue properties of the tungsten-based alloys IT180 (W-3.5Ni-1.5wt%Cu) and D176 (W-5Ni-2.5wt%Fe) have been determined using constant amplitude stress-controlled fatigue tests. These tests were performed at room temperature at relatively high cycle fatigue lives. The results indicate that the endurance limit for the alloys is about 210 MPa for IT180 and 425 MPa for D176. The fatigue strength coefficients and fatigue strength exponents are $S'_f = 1048MPa$ and $b = -0.11$ for IT180 and $S'_f = 3000MPa$ and $b = -0.13$ for D176. Strain-controlled fatigue tests were also performed to complement the stress-controlled experiments. The Multiple Step Test method was used to estimate the cyclic stress-strain curves of the alloys. The tests indicate hardening of both materials when subjected to cyclic loading. The cyclic strain hardening exponent of D176 was possible to find and was estimated to $n' = 0.08$. The fatigue response of the material is strongly affected by surface roughness, residual porosity, pore size and pore distribution. A finite element analysis was made to understand the effect of specimen geometry on the fatigue data. The results showed that specimen geometry affects stress concentrations and stress distribution, which might be related to the failure of the specimen. Scanning electron microscopy and energy dispersive spectroscopy have been used to characterize the sample's microstructures and fracture surfaces.

Acknowledgements

(Master Thesis student in Material Engineering Department) for his interest in our project whose questions made us consider different interesting points of view.

Table of Contents

List of tables

List of figures

Chapter 1 Introduction

1.1 The European Spallation Source Scandinavia

The European Spallation Source (ESS) Scandinavia is a joint European project, like that of many large-scale research facilities such as CERN in Geneva. The city of Lund in Sweden was chosen to be the host of ESS for being among the most scientifically developed regions worldwide. Currently the ESS is in the pre-construction phase which includes, among other things, the design of the target station. When it is finished in 2025 it is expected to be the world's leading research center using beams of slow neutrons. ESS can be compared to a large microscope, where neutrons are used to probe various materials.

In this sense the field of research will cover a wide range of disciplines such as: chemistry, nano and energy technology, environmental engineering, food technology, bioscience, pharmaceuticals, IT, materials and engineering science and archaeology [1-3].

1.2 Problem definition

The spallation source will produce neutron beams for scattering experiments by using an accelerator system to generate high-energy protons, which then knock out neutrons from a target (a so-called spallation process) [1]. The ESS targets have to withstand a large average beam power and are submitted to a combined load of high radiation damage, large temperature gradients and stress waves. In this context, the target material has to withstand all these conditions. ESS on this phase of the project is evaluating tungsten and tungsten heavy alloys as candidates for being target materials. The alloys combine the high density and high elastic stiffness provided by the tungsten with the mechanical properties of the alloying elements, especially relatively high ductility at room temperature that facilitates, among other things, the machinability of the tungsten and reduces the costs of production. The understanding of the different physical, mechanical and chemical properties of the target material is vital in the design stages of the ESS target station.

1.3 Relevance of the present work

More specifically, the materials to be studied in this work are the Tungsten Heavy Alloys (WHA) Inermet 180 (W-3.5Ni-1.5%wtCu) and Densimet 176 (W-5Ni-2.5wt%Fe).

Previous research have been related to the behavior of WHAs under tensile loading, as well as to microstructure and fracture surfaces under such conditions, and can be found elsewhere in literature. However, little research has been carried out to characterize the fatigue properties of WHAs and no work has been done specifically for Inermet 180 (IT180) and Densimet 176 (D176) in this area of research. The study of their fatigue behavior is of interest since high power targets undergo large and changing energy deposition densities, varying in space and time. As a consequence of this, high temperature fluctuations are induced, leading to very short and high cyclic thermal stresses in the target material. The obtaining of fatigue properties of IT180 and D176 is a preliminary research that can form a baseline for further investigations on, for example, the thermo-mechanical fatigue response once the target material is definitely chosen.

1.4 General Objectives

The scope of the present Master's Thesis is to characterize the fatigue properties of Inermet 180 and Densimet 176 and to study the behavior of these alloys under cyclic loadings by performing stress-controlled and strain-controlled fatigue tests.

1.4.1 Specific Objectives

-Determine the relationship between the fatigue life and the stress levels in the relatively high cycle fatigue regime by estimation of the Stress vs. Cycles to failure curve.

-Description of the cyclic response of IT180 and D176 under cyclic loading by the estimation of the Cyclic Stress-Strain curve.

-Comparison between the cyclic and monotonic responses of the alloys.

-Characterize the variables that affect the fatigue behavior of IT180 and D176.

-Description of the fracture surface and fracture mechanisms of these alloys.

-Study specimen geometry effects and how they may be related to the fatigue response of the materials.

1.5 Limitations

At the start of the project, samples for fatigue testing of each alloy were provided by ESS. However, due to budget issues and the interest of just a preliminary study of the alloys as a baseline for further decisions on the target material, the number of specimens provided was very small, making difficult in planning experiments for obtaining precise and vast information of the fatigue properties of the materials. Specifically, 21 specimens of IT180 and 12 specimens of D176 were provided. The main difficulty comes with the estimation of a *S-N* (stress to number of cycles to failure) curve that could describe the fatigue behavior of the materials with accuracy over the entire range of low-cycle and high-cycle fatigue. According to literature and fatigue standards, at least 6 specimens should be tested to obtain a preliminary estimate of the fatigue life [4], and a minimum of 15 specimens are recommended to estimate the fatigue limit [4-5].

Also, the specimens presented considerable surface roughness in the as-received condition. So, in order to fulfill the requirements about the specimens conditions established in fatigue standards (ASTM), grinding and polishing was carried out at the expense of a reduction in the testing section diameter.

The study of the surface of the Densimet 176 specimens with optical microscopy was performed but no digital images were recorded since the software used for this purpose stopped working before finishing this Thesis.

Chapter 2 Theoretical background

2.1 Tungsten Heavy Alloys

Tungsten heavy alloys are microcomposites of spherical tungsten grains in a continuous ductile matrix of, typically, nickel and iron or nickel and copper, bonding the grains together. The typical tungsten content varies from 90 to 98wt% [6-8].

2.1.1 Production of Tungsten Heavy alloys

The common procedure for the production of WHAs is liquid phase sintering. This procedure enables achieving an almost theoretical density by the considerable shrinkage during sintering as compared to the density obtained with only powder compaction. A brief explanation of how the sintering is carried out reads as follows:

Elemental powders are blended and then compressed using any common P/M blending and compressing procedure. The finer the W particles, the more homogeneity can be achieved. The W-particles range in size between 2-8μm [6]. In the case of iron and nickel alloys, carbonyl powders are used whereas fine electrolytic powder is used for nickel and copper alloys. The compacted material is sintered in a furnace with an atmosphere of pure hydrogen in the most general case; nitrogen mixtures, dissociated ammonia or just vacuum can also be used. The sintering of tungsten alloys can take place because of the difference in melting temperatures of the original powder components. When heating starts, the alloying elements will melt but, due to the high melting point of tungsten, this element will remain in a solid state. The melt is called the liquid-phase and flows between the tungsten particles, wetting them.

W-particles vary in size and since there is a limited solubility of the liquid phase in the solid, the smaller particles will solve in the melt until the final composition of the matrix is set, i.e. the liquid phase reaches saturation. With continued time at elevated temperature, once solved tungsten particles start to precipitate from the liquid-phase and diffuse into the still solid tungsten particles, coarsening them and making them grow. Final diameter of tungsten grains range from 50 to 150μm [8]. It is worth mention that, even though almost full theoretical density can be achieved by sintering, there will always be a presence of porosity in the final product, making the obtained density lower.

In general, the mechanical properties of WHA are strongly influenced by the final tungsten grain size, shape and contiguity. These are, at the same time, influenced by the tungsten content, sintering temperature and time [8-9].

2.2 The fatigue concept

When a repeated load is applied to a component it produces variable tensions, which in the long run can make the element brake at a lower load than it would have broken if exposed to a constant tension. The repeated loads produce cyclic stresses that are generally described in a sinusoidal waveform using three parameters: the stress range, S_r, the stress amplitude, S_a, and the mean stress, S_m, as shown in figure 2.1 [10].
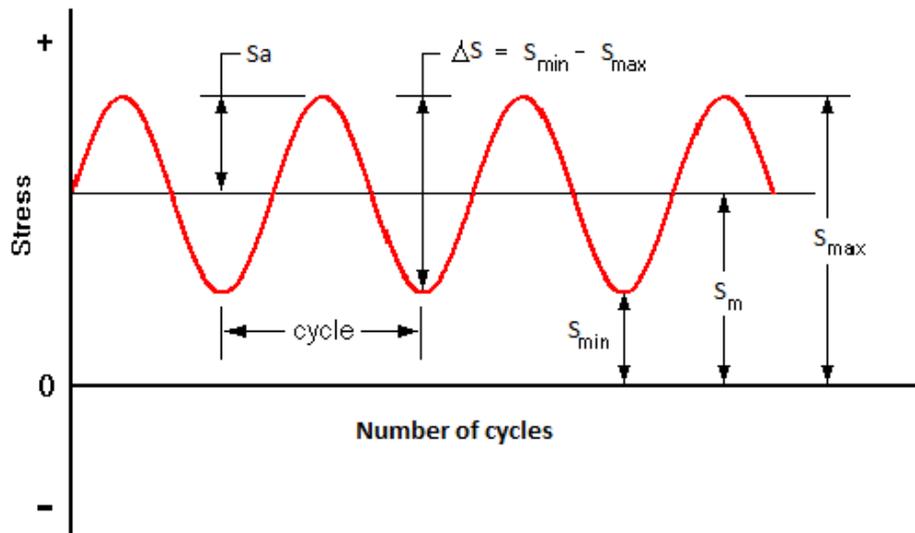
Figure 2.1 Cyclic stress variation with time and nomenclature for stress parameters which affect fatigue life.

The stress range is defined as the difference between maximum stress S_{max} and minimum stress S_{min} while the stress amplitude is a half of stress range. The mean stress would be one half of the algebraic sum of the maximum and minimum stresses.

$$S_r = S_{max} - S_{min} \qquad\qquad (2.1)$$

$$S_a = \frac{S_r}{2} = \frac{S_{max}-S_{min}}{2} \qquad\qquad (2.2)$$

$$S_m = \frac{S_{max}+S_{min}}{2} \qquad\qquad (2.3)$$

In fatigue testing, the stress amplitude or range is the controlled variable, and the number of cycles is the dependent variable. It has to be said that usually the tensile stresses are considered positive and the compressive ones, negative.

The fatigue life (N) is defined as the number of cycles to failure. Each cycle contains two reversals $(2N)$.

One of the most common fatigue routine tests is the uniaxial fatigue test using fully reversed loading, where the maximum and minimum stresses are equal in magnitude, i.e. the mean stress is zero. However, a zero mean stress situation is not always representative in many applications so some parameters are introduced to express the mean stress applied to the object. First of all, the stress ratio R represents the mean stress as the ratio of minimum stress to maximum stress (Eq. 2.4). Then the amplitude ratio A is defined as the ratio of stress amplitude to mean stress (Eq. 2.5).

$$R = \frac{S_{min}}{S_{max}} \qquad\qquad (2.4)$$

$$A = \frac{S_a}{S_m} = \frac{1-R}{1+R} \qquad\qquad (2.5)$$

Static loads have an $R = 1$ while the fully reversed loading means that $R = -1$.

2.3 Stress-life approach

The stress-life approach was firstly introduced by Wöhler between 1852 and 1870. His work gave the idea to obtain the fatigue response of a material from tests where cyclic loads are applied to a specimen of interest. Loads used can be plane bending, rotating bending, multiaxial or uniaxial tension and or compression, among others.

One of the most common tests, and the one used in this Thesis work is the application of uniaxial and equal tension-compression loading to a smooth specimen until failure finally occurs (the failure criteria would be the rupture of the piece). This kind of testing is called constant amplitude, fully reversed fatigue testing and data from such an experiment is used to plot the stress amplitude S_a against the number of cycles to failure N. This plot is called the stress-life or S-N curve. As it can be seen in figure 2.2, the life of a material increases when decreasing the stress amplitude until it reaches a certain point where a plateau is reached and stresses below this level do not cause

failure of the piece or component. The region above this point is called the finite life region while the plateau level is called the endurance limit S_e or fatigue limit, and is for most materials typically beyond about 10^6 cycles. The value of S_e is 35% to 50% of the tensile strength for most steels and copper alloys [11]. However, many high strength steels, aluminum alloys and other non-ferrous materials do not have a constant endurance limit. Instead a continuous increase in life is observed with lowering of the stress. In these cases, the endurance limit is considered to be the stress amplitude at 10^7 cycles since, from this point, the variation of N with the stress level is less compared to that in the finite life region [11].

Figure 2.2 Typical *S-N* curve of a material.

The stress life approach is most used in cases of High Cycle Fatigue (HCF, *N* above about 10^4) [12], where low stresses are applied and almost all the deformation taking place is elastic.

When the experimental data instead are plotted in a log-log scale, the curve becomes a straight line, and thereby a linear relationship between the stress amplitude and the fatigue life can be determined. This relationship was expressed by Basquin under the equation:

$$S_a = S'_f(2N)^b \tag{2.6}$$

Where S'_f and b are the fatigue strength coefficient and exponent, respectively. It is easy to deduce that once these two values are known for a specific material, its fatigue

behavior (at least at HCF) can be represented. Then, one of the scopes of this thesis is to determine S'_f and b for both tungsten heavy alloys.

2.3.1 The median curve

The fatigue life or behavior of a material cannot be estimated with complete accuracy, and a large number of specimens should be tested in order to obtain a fairly accurate S-N curve. The main reason for this is the inherent scatter in the fatigue properties of a material. Hence, statistical analyses need to be performed and reported along with the experimental data obtained to overcome the scatter problem and to be able to report reliable information to design engineers.

In this sense, the median S-N curve is a statistical way of presenting fatigue data and shows the fatigue behavior of 50% of all the population of samples tested. In other words, 50 out of 100 specimens tested are expected to fail at a certain N on the median curve when exposed to a given load.

It is worth to mention that scatter in fatigue properties will always be present while analyzing the test data. This might be due to several factors, for example differences in microstructure of specimens from the same batch (even if they were manufactured equally) can lead to different results despite testing at equal conditions [11], [13].

How to obtain the median S-N curve will be explained further in this chapter.

2.3.2 The mean stress effect

The mean stress level is known to play an important role in influencing the engineering materials behavior when subjected to fatigue loading [11]. In the high cycle fatigue regime, normal mean stresses are responsible for the opening and closing of microcracks. In this sense, tensile mean stresses are detrimental to fatigue strength since they contribute to crack growth whereas compressive mean stresses would be beneficial since they retard the cracks [13]. However, this effect is not that strong in the low cycle fatigue regime in which the large amounts of plastic deformation erase effects of a mean stress.

There are different models to calculate the stress amplitude taking into consideration a mean stress different from zero. These models are based on the stress amplitude at

zero mean stress. Three of them are commonly used: The Soderberg relation (Eq. 2.7), the Modified Goodman relation (Eq. 2.8) and the Gerber relation (Eq. 2.9).

$$S_a = S_a|_{S_m=0} \left\{ 1 - \frac{S_m}{S_y} \right\} \tag{2.7}$$

$$S_a = S_a|_{S_m=0} \left\{ 1 - \frac{S_m}{S_{TS}} \right\} \tag{2.8}$$

$$S_a = S_a|_{S_m=0} \left\{ 1 - \left(\frac{S_m}{S_{TS}} \right)^2 \right\} \tag{2.9}$$

S_a is the stress amplitude denoting the fatigue stress for a nonzero mean stress, $S_a|_{S_m=0}$ is the stress amplitude for fully reversed loading, S_y is the yield strength and S_{TS} is the material tensile strength [22].

Equation 2.7 gives a conservative estimate of fatigue life for most engineering alloys. Eq. 2.8 provides quite close results for brittle metals, and Eq. 2.9 is generally good for ductile alloys.

In 1968 Morrow presented a modification of the Basquin equation to take into account the mean stress effect, resulting in:

$$S_a = \left(S_f' - S_m \right) \left(2N_f \right)^b \tag{2.10}$$

Where the term added to the original Basquin equation (Eq. 2.6) is S_m, the mean stress value. Here Eq. 2.10 will be used to investigate the difference between making the tests with zero and non-zero mean stress (30MPa will be used as mean stress in this work as the target material will be submitted to approximately this mean stress while operating).

2.3.3 S-N curve vs. service conditions
Even though *S-N* curves are obtained using fixed test conditions (e.g., fully reversed constant stress amplitude), that in fact are not necessarily the same conditions as the ones the component is going to experience, they provide a baseline of the fatigue behavior that can be used by engineers during the design stages. On the other hand, the *S-N* curve can be used as a reference condition and there are methods that

combine the data obtained from it with other conditions to adapt it to the service case. During service, parts are subjected to different random levels of stress that are known to eventually cause fatigue failure of the component. The aim for the design engineers is to prevent such eventual failure and it has been suggested that the total damage (final failure) that occurs is an accumulation of the damage caused during each level of cyclic stress. This can be calculated from the *S-N* curve (Cumulative theory). Explanation of this theory can be found elsewhere in the literature [11], [13].

2.3.4 Estimation of the S-N curve

2.3.4.1 The median curve within the finite life region

In this work statistical analysis of fatigue data will be performed using the procedure proposed by ASTM on their practice E739 [4]. The stress vs. cycle curve will be computed following the methodology suggested in this standard. Yet this practice is also applicable for the estimation of strain vs. cycle curves. Note that the results presented in the following chapters and the terminology used tries to go in accordance with ASTM standards referenced in E739 [14], [15].

The tests are carried out in the high cycle fatigue regime but at stresses above the suspected endurance limit so that they will fail at relatively shorter lives, i.e. number of cycles higher than 10^4 but less than 10^6, to ensure the endurance limit is not reached. The exact localization of the endurance limit will not be found in this Thesis since a lot of specimens are needed for this purpose, and they were simply not available. There are special methods for the estimation of the endurance limit among which the Staircase Method is the most popular. However, it is recommended to test at least 15 specimens for this purpose [5], [16].

Due to the unavoidable scatter present on fatigue data, the final stress-life fatigue curve of IT180 and D176 will be presented in terms of a median curve and its associated statistics. According to ASTM, statistical analysis applies when the given data can be reasonably assumed to be a representation of some specific, defined population or universe of material of interest (under specific test conditions), and it is desired either to characterize the material or to predict the performance of future random samples of the material. This goes in accordance with the principal objective of the present work, which is to characterize the fatigue behavior of the alloys in order

to predict the performance of future samples of the same material during service in the spallation device.

Fatigue life data obtained from the stress controlled fatigue tests, i.e. number of cycles N_i at a specific stress amplitude S_i during fully reversed axial loading until failure, will be plotted on a log-log scale where the relationship between the life of the specimen and the stresses experienced is expected to follow a straight line. For the notation, the subscript "i" denotes each sample tested whereas the total number of samples is n.

The intention is then finding a line that better describes the fatigue response of the material, i.e. the line of best fit, which will be determined by the maximum likelihood method as recommended by ASTM in [4].

The linear S-N relationship is represented by:

$$Log(N) = A + B \cdot Log(S_a) \qquad\qquad (2.11)$$

in which S_a is the stress amplitude and N is the fatigue life of the specimen in number of cycles.

The fatigue life N is the dependent (random) variable in S-N tests, whereas S_a is the independent (controlled) variable.

Even though the real distribution of the S-N curve is unknown it is assumed that the logarithms of the fatigue lives are normally distributed, that is, the fatigue life is log-normally distributed. This implies that the scatter in $Log(N)$ is assumed to be the same at low and high stresses (the variance of the log life is constant over the entire range of the stresses used in testing). However, this is just an assumption because it is known that the scatter in the logarithm of the life increases when decreasing the stress. Nevertheless, the use of a log-normal distribution for the S-N curve in metals has been used in countless of studies and it has also been proved to provide a good fit or description of the fatigue curve of materials [12].

Accordingly, the independent variable is denoted with X and the random variable is denoted Y. In this case $X = Log(S_a)$ and $Y = Log(N)$. However, this practice can be

applied to analyze other data, and X and Y can represent some other variables. Then, Eq. 2.11 can be written as:

$$Y = A + B \cdot X \tag{2.12}$$

The maximum likelihood estimators are as follows:

$$\hat{A} = \bar{Y} + \widehat{B} \cdot \bar{X} \tag{2.13}$$

$$\hat{B} = \frac{\sum_{i=1}^{n}(X_i - \bar{X})(Y_i - \bar{Y})}{(X_i - \bar{X})^2} \tag{2.14}$$

Where $\bar{X}$ and $\bar{Y}$ are the average values of the independent and dependent variables and calculated as follows:

$$\bar{X} = \sum_{i=1}^{n} \frac{X_i}{n} \tag{2.15}$$

$$\bar{Y} = \sum_{i=1}^{n} \frac{Y_i}{n} \tag{2.16}$$

n is the total number of specimens (the total sample size). Then the variance of the normal distribution for $Log(N)$ is

$$\sigma^2 = \sum_{i=1}^{n} \frac{(Y_i - \hat{Y}_i)^2}{(n-2)} \tag{2.17}$$

in which $\hat{Y}_i$ is $\hat{Y}_i = \hat{A} + \hat{B} \cdot X_i$ and represents the estimated value of Y using the calculated estimators $\hat{A}$ and $\hat{B}$. The $(n-2)$ term in the denominator is used instead of n to make σ^2 an unbiased estimator of the normal population variance.

On the other hand, taking the logarithm of both sides of Basquin's equation (Eq. 2.6) and rearranging the terms, the following equation can be obtained:

$$Log(N) = -\frac{1}{b} Log(S'_f) + \frac{1}{b} Log(S_a) \tag{2.18}$$

Then, by comparing the latter equation with Eq. 2.12, it can be concluded that if $Y = Log(N)$ and $X = Log(S_a)$, the estimators would be $\hat{A} = -\frac{1}{b} Log(S_f)$ and $\hat{B} = \frac{1}{b}$.

Thereby, the values of the strength coefficient and the strength constant can be deduced as:

$$S_f^{'} = \exp\left(-\widehat{A} \cdot b\right) \qquad (2.19)$$

$$b = \frac{1}{\widehat{B}} \qquad (2.20)$$

2.3.4.2 Design curve (lower safety band)

A design curve is a line that characterizes the minimum fatigue life at a given fatigue stress level so that the majority of the fatigue data fall above this minimum or lower bound value. This line can be obtained by taking the median *S-N* curve and shifting it to the left by a constant value times the standard deviation. Hence the design curve can be estimated as:

$$Y_l = Y - K \cdot \sigma \qquad (2.21)$$

Where Y_l is defined as the lower limit of Y at a given X_i, σ is the standard deviation and K is a multiplier whose value varies depending on the design curve methodology chosen. The ASTM methodology suggests the use of a hyperbolic double sided confidence band as a design curve. However, they agree on the use of confidence and tolerance bands parallel to the fitted median *S-N* line. On the other hand, the choice of a lower tolerance limit is arbitrary and dependent on materials cost, safety policy and industry standards [13]. Based on all these circumstances and for the sake of simplicity, the design curve will be estimated using the Owen one-sided tolerance limit found in reference [13] where the constant value K is approximated by K_{owen}.

The design *S–N* curve then can be expressed as follows:

$$Y_{R95C90} = Y - K_{OWEN} \cdot \sigma \qquad (2.22)$$

The K value is derived from the following expression:

$$K_{OWEN} = K_D \cdot R_{OWEN} \qquad (2.23)$$

Where:

$$K_D = c_1 \cdot K_R + K_C\sqrt{c_3 K_R^2 + c_2 a} \qquad (2.24)$$

$$R_{OWEN} = b_1 + \frac{b_2}{f^{b_3}} + b_4 \exp(-f) \qquad (2.25)$$

In which

$$K_R = \varphi^{-1}(R) \qquad (2.26)$$

$$K_C = \varphi^{-1}(C) \qquad (2.27)$$

$$f = n - 2 \qquad (2.28)$$

$$a = \frac{1.85}{n} \qquad (2.29)$$

Here $\varphi\,(\cdot)$ is the standard normal cumulative distribution function. The empirical coefficients b_1, b_2, b_3 and b_4 as well as c_1, c_2, and c_3 are tabulated in appendix B.

The values of C and R are the Confidence level and the Reliability, respectively. For example, when the notation $R95C90$ is used for design purposes, that value ensures that there is a 95% chance of survival with a 90% of confidence level for a fatigue life at a specified fatigue level [9]. In this Thesis values of C=90% and R=95% will be used.

It was decided to use K_{owen} because it takes into account the sample size and also allows to use any reliability value higher than that of E739 (R50%).

2.3.4.3 Sampling for strain-controlled testing
Standard practice E739 recommends a minimum number of specimens to be tested depending on the purpose of the research. This is summarized in Table 2.1.

Table 2.1 Minimum of specimens required depending on the type of test program to be carried out.

Type of Test	Minimum of specimens
Preliminary and exploratory (exploratory research and development tests)	6 to 12
Research and development testing of components and specimens	6 to 12
Design allowable data	12 to 24
Reliability data	12 to 24

On the other hand, when performing tests where statistics is involved, the more specimens tested, the better the reproducibility of the results. In this sense ASTM

proposes replication guidelines which depend on the number of stress levels and the number of specimens tested at each level. Table 2.2 shows the ASTM replication recommendations.

Table 2.2. Percentage of replication depending on the type of test program to be carried out.

Type of Test	Percentage of replication
Preliminary and exploratory (exploratory research and development tests)	17 to 33
Research and development testing of components and specimens	33 to 59
Design allowable data	50 to 75
Reliability data	75 to 88

The percentage of replication is calculated as:

$$\%Replication = 100\left[1 - \frac{Total\ number\ of\ different\ stress\ levels\ used\ in\ testing}{Total\ number\ of\ specimens\ tested}\right]$$

The percent replication indicates the portion of the total number of specimens tested that may be used for obtaining an estimate of the variability of replica tests.

2.4 Strain-Life approach

In contrast to the stress-life approach, this methodology for describing the fatigue behavior of a component uses the local strain as the governing fatigue life parameter. As mentioned, the stress-life approach is suitable in cases of low stress magnitudes where the major part of the deformation is elastic. However, there are cases of high stresses where plasticity is present. Furthermore there are also situations where, even when the component appears to have nominally cyclic elastic stresses, local plastic deformation can be present (stresses can locally exceed the yield stress) in areas of stress concentrations such as at welds. In this context, the use of a strain-life approach is recommended and has been shown to be more effective in the prediction of the fatigue life [13].

The results from strain-controlled tests are generally used to plot the strain-life relationship, where the number of cycles to failure is plotted against the corresponding strain levels. A statistical analysis can be performed similar to what applies to the stress-life curve. The results can then be combined to obtain the entire curve. However, the estimation of the strain-life curve is out of the scope of this Thesis since just the relationship between the applied stress and the fatigue life is of interest, specifically at relatively low stresses which can be estimated by performing stress-controlled tests. Still, strain-controlled testing also allows estimating the cyclic stress-strain curve of the material by applying fully reversed constant strain amplitudes. According to Jones and Hudd [17] it is then necessary to derive the cyclic stress-strain curve of the material, since the information provided by a monotonic curve is just an approximation, especially when significant hardening or softening takes place.

2.4.1 Material response under cyclic loading

Under constant amplitude strain-controlled fatigue loading, the stresses in the material varies with each reversal during the initial cycles. This initial stage of change in resulting stress amplitudes is known as the transient cyclic response of the material and describes how the resistance to deformation changes due to cyclic loading. In this respect, the material can behave in one of the following manners: cyclic hardening, cyclic softening, remain stable or a combination. In the case where there is transient cyclic hardening, the flow stress will increase with increasing number of cycles. In transient cyclic softening the flow stress is lowered at each successive cycle. However, the rate of change in stress in both scenarios decreases with number of cycles, and after a certain number of cycles the material reaches a steady-state, where the stress remains almost constant despite continuous cycling, i.e. the material stabilizes and it is said that it has reached saturation. Once steady state is reached, it can be observed by plotting the stress versus the strain amplitude. The resulting plot, shown in figure 2.3, is known as the hysteresis loop of the material and represents the elastic plus plastic work under cyclic loading. The stress at which the hysteresis loop stabilizes at a given strain amplitude is called the peak stress. In this sense, if a group of stabilized hysteresis loops at different strain levels are plotted, a cyclic stress-strain curve can be obtained by joining of the peak stresses of each loop as shown in figure 2.3.
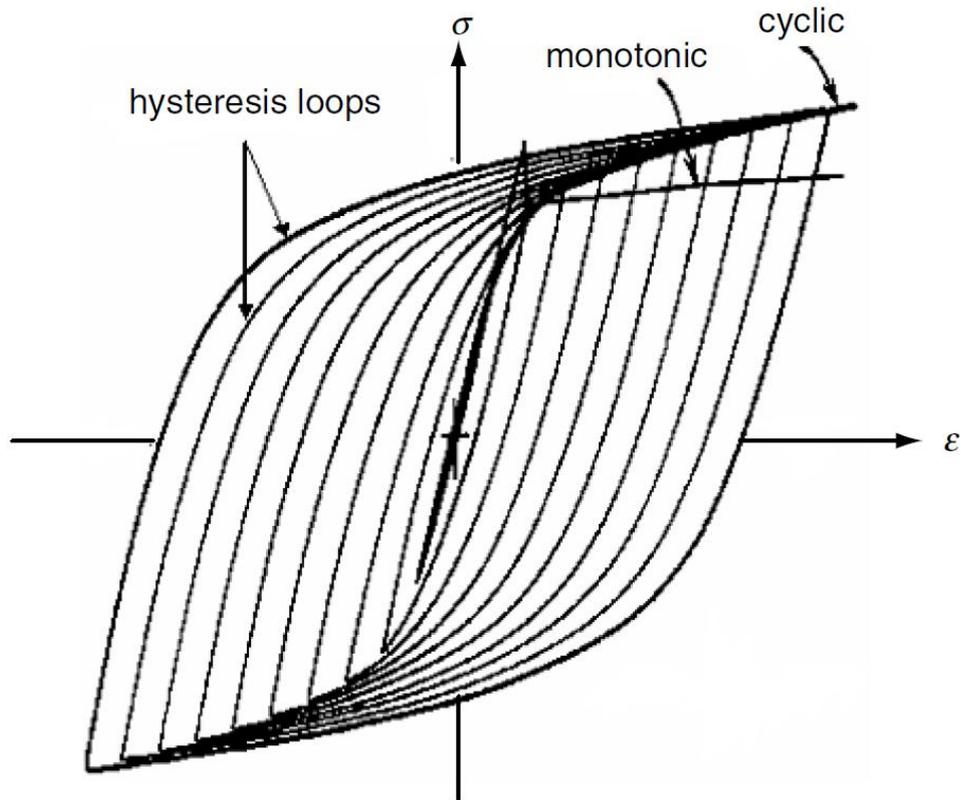
Fig. 2.3 Hysteresis loops at different strain levels and the cyclic stress-strain curve formed by joining the locus of the loop tips. The tensile curve is superimposed in the figure to show the relationship between the cyclic and monotonic behavior of the material. (Figure extracted from reference [13].)

2.4.2 Cyclic vs. Monotonic behavior

The Cyclic Stress-Strain (CSS) curve reflects the resistance in a material to cyclic deformation and can be different from the monotonic stress–strain curve. Commonly these two curves are compared by plotting them in the same graph and observing if the material under cyclic conditions hardens, softens, remains stable or has a mixed behavior compared to that under a monotonic tensile situation.

When the true stress vs. the true strain from a tensile test is plotted, the curve is approximately described by the Ramberg-Osgood relationship as [11] [13]:

$$\varepsilon = \frac{\sigma}{E} + \left(\frac{\sigma}{K}\right)^{1/n_m} \tag{2.30}$$

Where σ is the true stress, E is the Young's modulus, ε the total true strain, K is a constant called the monotonic strength coefficient and n_m is known as the monotonic strain hardening exponent.

The total strain experienced by the material can be decomposed in the elastic and the plastic parts, then:

$$\varepsilon_e = \frac{\sigma}{E} \qquad (2.31)$$

$$\varepsilon_p = \left(\frac{\sigma}{K}\right)^{1/n_m} \qquad (2.32)$$

where ε_e and ε_p are the elastic and plastic strains, respectively.

Similarly, the resulting CSS from the strain controlled test can be described by:

$$\varepsilon_a = \frac{\sigma_a}{E'} + \left(\frac{\sigma_a}{K'}\right)^{1/n'} \qquad (2.33)$$

The latter expression is based on Masing's assumption (Masing, 1926) found in references [13], [18]. Here σ_a is the stress amplitude, E' is the Young's modulus, ε_a the strain amplitude, K' is the cyclic strength coefficient and n' is known as the cyclic strain hardening exponent. The CSS is plotted using the values of the stress and the strain amplitudes of the stabilized hysteresis loops, which commonly are taken at half of the fatigue life.

The material constants K' and n' can be estimated as the intercept and slope of the line that best fits the plastic strain vs. stress amplitudes in a log-log scale of the form:

$$\sigma_a = K'\left(\varepsilon_p\right)^{n'} \qquad (2.34)$$

Or, in an equivalent form:

$$Log(\sigma_a) = Log(K') + n'Log(\varepsilon_p) \qquad (2.35)$$

The former has a similarity to Eq. 2.12, and the statistical analysis presented in ASTM standard practice E739 and explained in section 2.2 allows to estimate K' and n' as in reference [9]. In this case, the statistically independent variable is the plastic strain amplitude and the statistically dependent variable is the stress amplitude. In other words: $Y = (\sigma_a)$ and $X = Log(\varepsilon_p)$. An equivalent procedure applies for the estimation of the monotonic parameters K and n_m. The typical range of n_m for alloys is 0-0.5, and for n' 0.1-0.2 [13].

The plastic strain amplitudes are calculated as:

$$\varepsilon_p = \varepsilon_a - \frac{\sigma_a}{E'} \qquad\qquad (2.36)$$

Where ε_a is obtained from the strain-controlled fatigue test.

It has been mentioned that the materials during the spallation process undergo low stress amplitude cyclic loading and are expected to have a long life; hence information at high cycle fatigue is of main interest. However, since the aim of this research is to characterize, as much as possible, the behavior of both WHAs under fatigue conditions it was decided to perform strain controlled testing as well.

2.4.3 Estimation of the Cyclic Stress Strain curve

Strain controlled tests have gained increasing interest in the determination of CSS curves for engineering alloys [11]. There are three common strain-controlled methods to obtain the CSS curve which differ in the number of specimens needed for testing and, hence in the time needed for the procedure. These methods are listed below and shown in figure 2.4:

-Constant Strain Amplitude Method or Companion Specimen Test (CST): the specimen is cycled within a constant strain limit until failure occurs. Multiple specimens are needed, each tested at a separate strain level in order to obtain the CSS curve from their resulting stabilized hysteresis loops.

-Multiple Step Test (MST): a specimen is cycled at a constant strain level until a stable hysteresis loop results. Then the strain level is increased until stabilization again takes place. The strain level is increased until the entire CSS curve is obtained by using just one specimen.

-Incremental Step Test (IST): the specimen is subjected to blocks of increasing and decreasing strains until the stress at each level of strain becomes constant. The resulting stable hysteresis loops provide the CSS plot.

Method	Strain waveform
Constant Strain Amplitude	
Multiple Step Test	
Incremental Step Test	

Figure 2.4 Test methods for obtaining the cyclic stress-strain curve. The multiple step test method is the one used in this work.

The methods that require just one specimen are often used by investigators and after doing literature research these authors found reports were one specimen tests have been used successfully, such as in references [17], [19-21]. Researches with different materials have observed differences in CSS curves obtained by each method [17], where the differences could be explained by the dislocation substructures generated, depending on the actual strain history. The cyclic strain rates might also influence since the tests can be performed using either constant strain rate or constant frequency, in which case the strain rate increases with increasing strain amplitude. However, the results from the MST and the CST should be similar and this was found in the study of low carbon steel done by Polak et. al [20]. The latter gives a very good approximation of the cyclic stress-strain curve of the material with a long saturation stage. Considering this, and for facilitating the testing procedure, the MST was the method chosen for this work for the estimation of the CSS curves of IT180 and D176.

2.5 Loading situation of the specimens

2.5.1 Stress concentrations

When an axial force is applied to a member, the stress distribution created is not uniform, but a complex stress distribution appears along the character. In figure 2.5 it can be seen that at the top of the member, where the force P is applied (1), some distorted lines are present. Then, at the middle of the character (2), the lines are straight because they are away from the load and support, and, finally, at the bottom (3) distorted lines also appear, caused by the support [22].
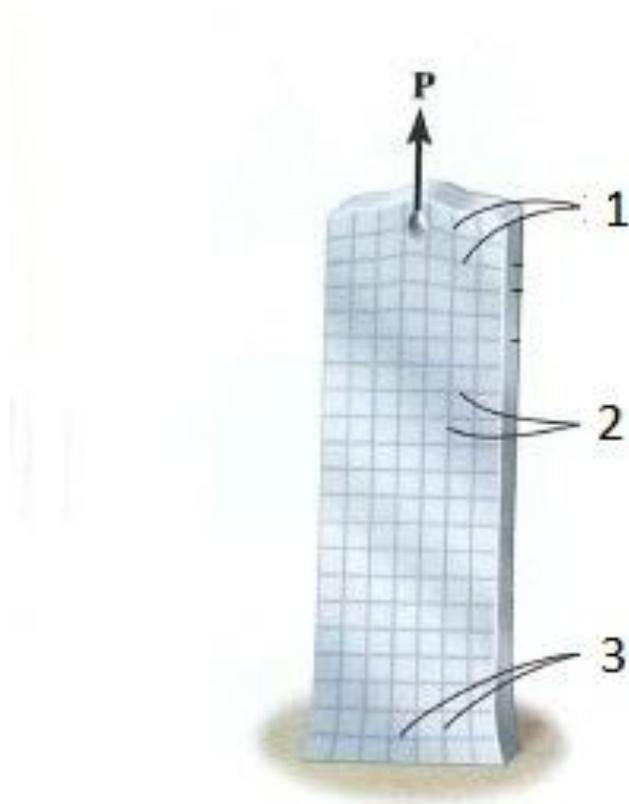
Figure 2.5 Localized deformation when a force P is applied on a member. (Figure extracted from reference [22])

The stress concentrations not only appear in this situation, but they are also present where the cross-section area changes. The maximum normal stress will occur at the smallest cross-section area, and this is what the engineering practice takes into account instead of determining the entire stress distribution when designing. On the other hand, if the material is brittle or if it will be subjected to fatigue loading, the stress distribution becomes important. In IT180 and D176 samples this maximum

stress could be placed in any cross-sectional plane of the sample neck (in the gage area), which is the part of the sample with the smallest cross-sectional area. Moreover, a deeper study will be carried out to find where the stress concentrations appear.

When calculating stress concentrations, the stress-concentration factor, K_t, is commonly used. This is defined as:

$$K_t = \frac{\sigma_{max}}{\sigma_{avg}}$$

(2.37)

where σ_{max} is the maximum stress and σ_{avg} is the average stress acting over the smallest cross section. σ_{avg} is calculated as the load P divided by the smallest cross-sectional area. The K_t value depends only on the specimen geometry and the type of discontinuity.

Regarding the specimens geometry, sharp corners and close radii should be avoided, because in those areas high stress concentrations appear. For brittle materials, the stress limit for no failure may be at the rupture stress, so for these materials failure will be obtained as the yield stress is reached. The crack will initiate and propagate through the cross section, resulting in sudden fracture of the member.

2.5.2 Residual stresses

When compressive and tensile stresses are applied to a member, residual stresses can remain after the stresses are removed. When unloading, there is an elastic recovery in the material which can cause permanent deformation while the material tries to recover plastic strain. Such residual stresses caused by fatigue, and also by machining and treating of the material, affect the material fatigue life.

Chapter 3 Experimental work

3.1 Specimens for testing

3.1.1 Specifications

Tungsten heavy alloys samples were received from Plansee, the supplier. In figure 3.1 a 3D image of the sample, modeled with SolidWorks, and a plan with the sample dimensions are shown.
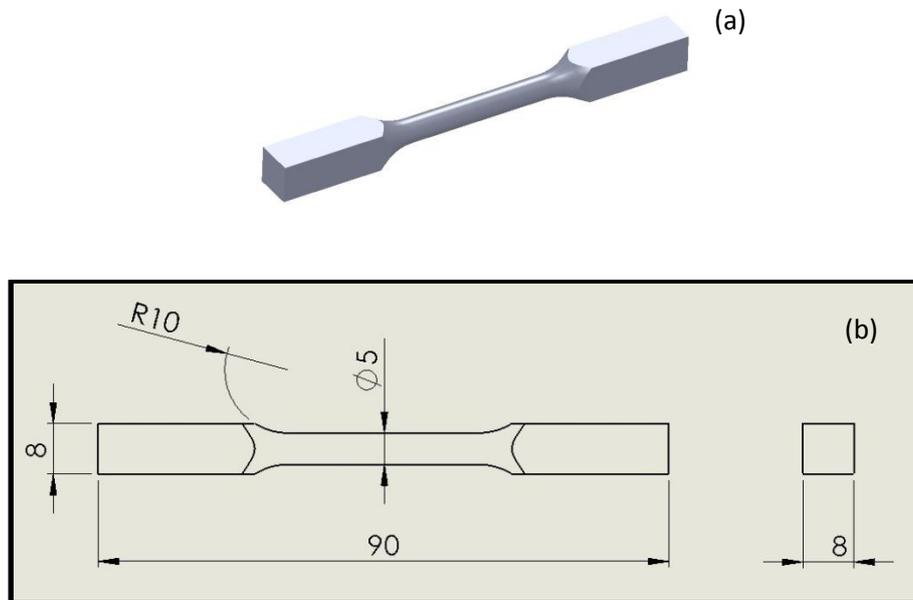
Figure 3.1 Sample modeled with SolidWorks; (a) 3D view, (b) sample dimensions in mm.

The specimen geometry was designed so it could adapt to the testing machine available at the LTH laboratory. However, reviewing ASTM standard practices to perform stress and strain controlled fatigue tests and tensile tests [4], [18], [23], [24], some differences were noted between their recommendations for the specimen geometry, preparation and storage and the received specimen's conditions. These remarks are worth mention since they might affect the fatigue data obtained and the reproducibility of the results.

- Geometry:

The specimen design should ensure that failure occur within the test section area. There are several possible specimen geometries but only that similar to our samples shall be discussed. In this sense, specifications for specimens with tangentially blended

fillets between the test section and the ends described in [23] are of interest. The uniform and circular gage section (testing section) should preferably have a diameter between 2.54mm and 5.08mm to ensure the test section failure. The grip area should be at least 1.5 times the test section area, but preferably 4 times larger. Standard practice E606 for strain controlled fatigue testing [18] suggests solid circular cross sections with a minimum diameter of 6.35mm. However, specific cross-sectional dimensions are listed there only because they have been dominant in the generation of the low-cycle fatigue database that exists in the open literature. Specimens possessing other diameters, or tubular cross sections, may be tested successfully within the scope of that practice; however, crack growth rate, specimen grain size, and other considerations might preclude direct comparisons with test results from the recommended specimens. It is observed in figure 3.1 (b) that the nominal testing section diameter of the specimens is 5mm, which already is lower than that suggested in practice [18]. Also, the specimens were ground and polished to fulfill the recommendations regarding surface conditions. As a consequence, the actual diameter of the test section in the samples was lowered down to 4.99±0.01mm. It was decided to carry out the surface machining under the consideration that a poor treated surface could be more detrimental to fatigue crack initiation than the effect of reducing the gage section diameter.

The test section length should be at least 2 times the test section diameter, especially to minimize buckling in compression. Samples with a continuous radius between the ends should have a curvature radius at least 8 times the test section diameter to minimize the theoretical stress concentration factor K_t [23]. In this case, the samples received did not accomplish to this, since the diameter in the test section was 5mm and the blend radius was 10mm, so the results may have been affected by this issue. As the specimen geometry may affect the fatigue and fracture behavior, a FEM analysis of the specimen geometry, explained in following sections, was performed to observe how the stresses are distributed and where they are concentrated. In general, special care has to be taken in low ductility materials which will be exposed to high stresses since this has been shown to be a factor important to the variability of the test results.

- Surface preparation:

As concerns the surface preparation, the specimens have a "surface preparation history" as a consequence of the machining processes, the heat treatments performed and the environmental conditions during storage. This can affect the fatigue behavior as well as the fracture behavior, so the influence from these factors should be minimized. A smooth and uniform surface should be obtained, and machining or finishing operations should be done to ensure minimal surface distortion. A better explanation of this is given later on in this chapter.

- Storage:

Oxidation and corrosion should be avoided by using protective atmospheres. The exact procedure of specimen storage should be clearly documented. The samples have to be stored in a suitable protective environment; in the present case the specimens were stored in a dehumidificator to prevent surface attacks. In the case of tungsten, special care has to be taken in this aspect, since this material has a high tendency to oxidize.

3.1.2 Inspection and preparation of the specimens:
Before performing a test, the specimen surface was inspected in the microscope at x20 magnification. According to ASTM standard practice [23], no roughness should be able to be seen at the surface at this magnification. However, all the samples in their "as received" condition presented clearly visible stripes, and in order to prevent this defect from being a source of micro-crack initiation, each specimen was ground and polished to obtain a smoother surface. After machining, great improvement in surface roughness was observed but thin radial lines, resulting from the manufacturing procedure, were still visible with x20 magnification. However, these lines were clearly thinner in width than before the surface preparation. The resulting decrease in the diameter of the samples was between 0.02-0.03mm. The fact that there was still presence of stripes provides an estimate of the depth of the roughness. Below figures 3.2 and 3.3 show the difference of the surface observed before and after the grinding and polishing.

On the other hand, another defect observed in the specimens was the presence of pores, which is a typical characteristic of materials obtained by powder metallurgy

processes. It was of interest to see if once ground and polished, the pores size could be decreased or even eliminated.
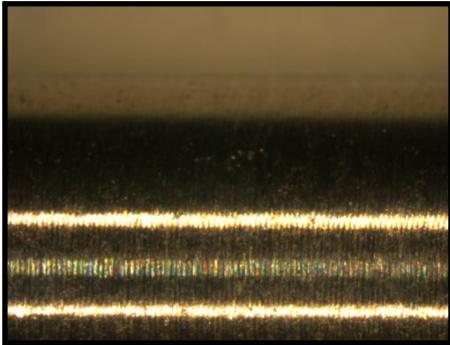
Figure 3.2 Surface of the IT180 sample seen at x20 magnification before grinding and polishing.
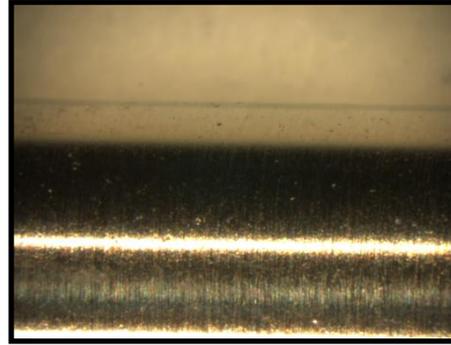
Figure 3.3 Surface of the IT180 sample seen at x20 magnification after grinding and polishing.

During the length of the project the optical microscope that allowed us to record digital images of the samples as well as measure the size of the porosity on the specimens was damaged. Even though the smoothness of Densimet 176 was checked after the grinding and polishing and every sample was inspected qualitatively, no digital images of the pores or surface of this alloy could be recorded.

3.1.3 Density calculations

The density of both alloys was theoretically and experimentally calculated using Archimedes' principle and the percentage of porosity have been calculated. Moreover, the experimental value can be compared with the values given by Plansee, the specimen provider. Tables 3.1 to 3.4 show the results obtained by calculating the theoretical density and measuring the density for 3 specimens of each alloy by Archimedes' principle.

Table 3.1 Results obtained by calculating the theoretical density for IT180

Elements	%weight	Theoretical Density [g/cm^3]	Density [g/cm^3]
W	95	19.25	17.29
Ni	3,5	8.908	0.64
Cu	1,5	8.96	0.28
TOTAL			18.2

Table 3.2 Results obtained by calculating the theoretical density for D176

Elements	%weight	Theoretical Density [g/cm^3]	Density [g/cm^3]
W	92.5	19.25	16.27
Ni	5	8.91	0.88
Fe	2.5	7.87	0.44
TOTAL			17.59

Table 3.3 Results obtained by calculating the experimental density for IT180

SPECIMEN	Mass(air)[g]	Mass(water) [g]	Density [g/cm^3]
7	41.49	39.19	18.04
9	41.47	39.17	18.06
8	41.71	39.40	18.06

Table 3.4 Results obtained by calculating the experimental density for D176

SPECIMEN	Mass(air) [g]	Mass(water) [g]	Density [g/cm^3]
6	40.75	38.44	17.64
9	40.46	38.15	17.55
10	40.53	38.21	17.50

The mean value for the experimental density of IT180 is 18.05g/cm^3 while for D176 it is 17.56g/cm^3. The values got from Plansee were 18.0g/cm^3 and 17.6g/cm^3, respectively, so the results obtained are correct. Then, the percentage of porosity can be calculated as, see Table 3.5:

Table 3.5 Percentage of porosity for each alloy.

Alloy	Porosity [%]
IT180	0.78
D176	0.19

As observed in the optical microscope, IT180 has higher porosity than D176.

3.1.2.1 Grinding and polishing procedure

The selection of grinding and polishing procedures was chosen in relation to the available facilities. First, the grinding was done using a sequence of grinding papers of 320, 500, 1000 and 4000 particles per square inch. Then, the sample was polished using 3µm diameter diamond (DP suspension). The specimen was observed in the microscope at x20 magnification and since some stripes were still visible, it was determined to polish again, but using a 1µm diameter diamond so that an even smoother surface was finally obtained.

3.2 Microstructural Examination

3.2.1 Preparation of the samples

Extraction of two small and perpendicular sections at the grip area of one specimen of each alloy that had been used during tensile testing was performed. These particular specimens were used under the belief that, since it had been subjected to tensile testing only, no notable difference in the microstructure should exist as compared to that of as-received samples. The sectioning was done with an aluminum oxide cut-off wheel (Φ=125mm) from Accutom for cutting hard ferrous materials (HV>500), see figure 3.4. Coolant was used to ensure an almost plane surface and avoid mechanical or thermal damage.

Figure 3.4 Struers Accutom-5 machine used for cutting.

Encapsulation of the samples was done in two layers of Struers compression molding resins. The bottom layer consisted of a bakelite hot mounting resin, and the top

consisted of a diallyphtalate hot mounting resin that facilitates the subsequent machining of the sample. The complete mounting of the sample was done in a Predopress Struers machine that preheats, heats, presses and cools the capsule so the resins can melt and solidify. The sample is seen in figure 3.5.
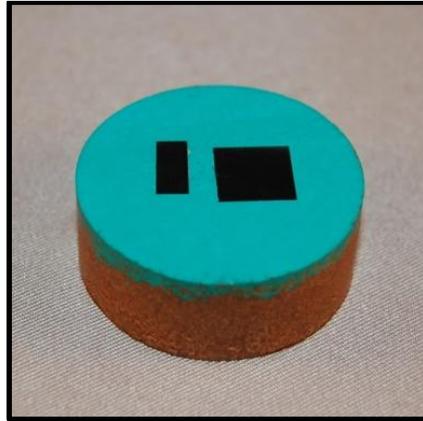
Figure 3.5 Sample used in the microstructural examination.

Grinding with a sequence of 320, 500, 1000 and 4000 particles per square inch of SiC paper followed by polishing with 3µm and 1µm diamond suspension were conducted using an abrasive rotating wheel, see figure 3.6. Cleaning of the specimen was finally performed and the specimen was then ready for inspection in the microscope.

Figure 3.6 Struers Rotopol-2 used for grinding and polishing.

3.2.2 Scanning Electron Microscopy (SEM) and Energy Dispersive Spectroscopy (EDS)

The SEM uses a high-energy beam of electrons to scan the sample surface in a raster scan pattern of rectangular or square form. The electrons scan the surface until they

escape from the material or are absorbed by it. A volume of the part that is analyzed with the incident beam is irradiated and different signals are generated, i.e. secondary electrons, back-scattered electrons and X-rays. Each of these signals varies in intensity depending on the properties of the material and the topography of the surface. Thus these intensities can be measured and allow to reconstruct the image and extract information about the surface and its properties.

Back scatter electrons were used in our work to analyze both the microstructures and the fracture surfaces of the materials of interest. X-rays were used for mapping of the microstructure by energy dispersive microscopy since these kinds of beams give characteristics of the atoms being irradiated. Hence information of the chemical composition of the different phases of the material could be obtained [25].
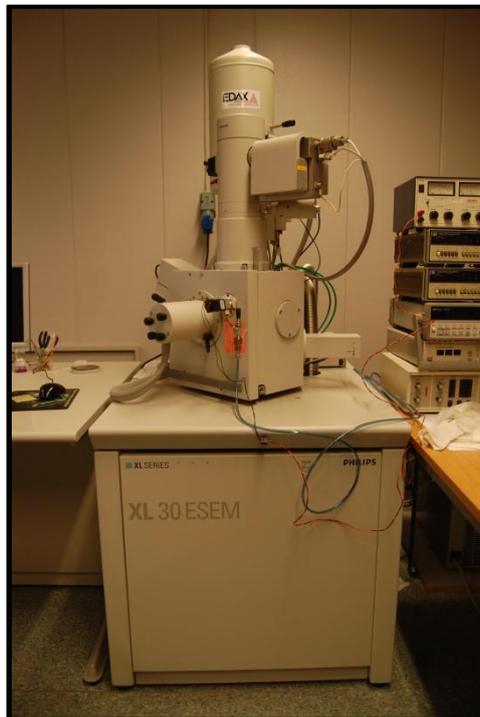
Figure 3.7 Philips XL 30 ESEM used to study the samples surface and fracture surfaces.

The prepared sample was put into the SEM, figure 3.7, and vacuuming of the chamber followed. The analysis used a 1.75A filament current and 20kV beam voltage.

3.3 Equipment needed for mechanical testing

A machine MTS Ramen (max. capacity 250kN, calibrated in May 2010) for tensile and fatigue testing have been used to perform both type of tests at the M building

laboratories at LTH. This machine is shown in figures 3.8-3.11. The control system connected to the machine is Instron Digital Electronic. The machine used has two grips, an upper one which is fixed, and a lower one that is responsible for the load application. When the test starts the upper grip holds the specimen in a fixed position while the lower grip applies the force. In the case of a tensile test the force is slowly increased until the specimen breaks. In the case of a fatigue test, a sinusoidal load with a frequency of 30Hz is applied until the specimen breaks and the machine stops. The machine has a hydraulic system that provides the pressure, 10bar, to hold the specimen by the grips.

Figure 3.8 MTS Ramen machine used for tensile testing and fatigue testing.

3.3.2 Preparations for the test

Firstly, the strain and load are calibrated and set to zero. It is necessary to align the specimens; otherwise multiaxial stresses could appear inside it and consequently falsify the results. To do so, a metal piece with three sensors, figure 3.9, is put between the grips, where the specimen will be put afterwards, and is held by the clamps. After the alignment is ready, the metallic piece with sensors is changed for the sample. In the case of a tensile test, an extensometer is placed in order to measure the elongation of the specimen. After this last step, everything is ready for running the test.

Figure 3.9 Metal piece with sensors used to align the specimen.

Figure 3.10 Sample ready for the test.

Figure 3.11 Extensometer used to measure the deformation in the tensile test.

3.4 Tensile test

First of all, in order to know the material behavior and some important properties necessary to do the fatigue tests, a tensile test was performed. In this case, two samples of each tungsten heavy alloy have been tested.

The tensile test consists in applying an increasing load in the specimen axial direction until final failure occurs, i.e. rupture of the specimen. With this kind of test, one can measure the material resistance to the application of a static load (or a slowly increasing one). In this case, the rate of elongation was set to 3mm/min (0.05mm/s).

Remark concerning the tensile test of IT180 on specimen #1: When the first test started there was a sudden stop of the machine due to a mistake in the configuration of the test equipment. There was a load control system on and it was activated because the pressure of the grips was less than the recommended (10bar). However, the test was restarted after setting the right pressure level (the sample was not removed and the machine was not calibrated again).

Remark concerning the tensile test of D176 on specimen #1: a default setting of the program was to stop the test after an elongation of 10mm. Since D176 is very ductile, the machine stopped before rupture of the piece.

Due to the inconveniences of both first tensile tests, a second specimen of each alloy was tested and the results from these tests on specimens #2 of the two WHAs are the ones used for the calculations.

3.5 Fatigue Tests

3.5.1 Stress-Controlled testing

As it was mentioned before, stress controlled fatigue testing has been performed. However, the entry parameter for the machine is the applied load and not the stress amplitude. Thus the equivalent load for each desired stress level has to be calculated. Being an axial load case the applied load P is calculated according to Eq. 3.1 below, where S_a is the stress amplitude and d the sample testing section diameter. It has to be said that the diameter is not exactly the same for all the samples because, as mentioned before, all the samples were prepared by grinding and polishing, and since this is a hand-made process the same diameter for all the samples could not be obtained after the surface treatment.

$$S_a = \frac{P}{A} \rightarrow P = S_a \cdot A \rightarrow P = S_a \cdot \pi \cdot \frac{d^2}{4} \tag{3.1}$$

The failure criterion is the complete separation of the piece and the number of cycles to run-out is set to $2 \cdot 10^6$ cycles.

IT180 was the first WHA to be tested. The strategy was to test at different stress amplitudes, trying at the same time to come as close as possible to the fatigue limit. In this sense, after the first test, if failure occurred then the next stress level would be lowered while it would be increased in case of no failure.

Keeping in mind that the Ultimate Tensile Stress (UTS) for this alloy is 631MPa and that the endurance limit for powder metallurgy materials usually is found at 30-40% of this value, the first test on specimen #3 for this alloy was run at a stress amplitude of 300MPa (about 50% of the UTS), expecting that the sample would fail, but not far from the fatigue limit. Failure occurred at 33831 cycles. In order to investigate the reproducibility of the results, a second experiment with specimen #4 was run also at 300MPa, and 40177 cycles of life were obtained. Afterwards, the stress amplitude was decreased to 200MPa, obtaining for specimen #5 an infinite life. In this case the specimen did not break even after $6 \cdot 10^6$ cycles, so it was decided to stop the test and consider it a run-out. This is why, both due to the time of testing (this last test run for

more than two days) and due to the fact that for most materials[1] the fatigue limit is reached beyond about 10^6 cycles, the fatigue life for a run-out was set at $2 \cdot 10^6$ cycles. One more specimen, specimen #6, was tested at 200MPa stress amplitude, and it did not brake either, so the test was stopped at $2 \cdot 10^6$ cycles. At this point, the endurance limit was situated clearly between 200 and 300MPa, so specimen #7 was decided to be run at 250MPa, obtaining 139854 cycles as a result. Next test was run at 225 MPa, and specimen #8 failed after 336042 of fatigue. Following 3 tests, specimens #9, #10 and #11, were run at 210MPa in a row, having as a result 312378, $2 \cdot 10^6$ and 1626921 cycles, respectively. At this point, the endurance limit was set around 210MPa for IT180. Finally two more specimens, specimens #12 and #13, were tested at 250 and 225MPa, breaking at 329748 and 424545 cycles, respectively. The results are summarized in Table 3.6.

Table 3.6 Stress amplitude that each specimen was exposed to, its diameter, the load and the cycles before failure for IT180.

Specimen	Stress [MPa]	Diameter [mm]	Load [N]	Life [cycles]
3	300	4.99	5866.95	33831
4	300	4.99	5866.95	40177
5	200	4.98	3895.64	6.00E+06
6	200	4.98	3895.64	2.00E+06
7	250	4.98	4869.55	139854
8	225	4.98	4382.59	336042
9	210	4.99	4106.86	312378
10	210	4.99	4106.86	2.00E+06
11	210	4.99	4106.86	1626921
12	250	5.00	4908.74	329748
13	225	5.00	4417.86	424545

---

[1] Value typical for mild steels and other materials which harden by strain-ageing [11].

Fatigue testing of D176 followed next. Run-outs of specimens #3 and #4 at 300 MPa and 400 MPA, respectively, were first obtained. Thereby specimen #5 was tested at a higher stress, 500 MPa, breaking at 958423 cycles. Next test with specimen #6 was run at 450 MPa, obtaining 885.444 cycles as a result. Then, 550 MPa was decided as the stress amplitude for the next test, and specimen #7 failed at 213838 cycles. Specimen #8 was run again at 450 MPa, obtaining 1468220 cycles as a result, and specimen #9 was run at 550 MPa, breaking at 258788 cycles. The results are summarized in Table 3.7.

Table 3.7 Stress amplitude that each specimen was exposed to, its diameter, the load and the cycles before failure for D176.

Specimen	Stress [MPa]	Diameter [mm]	Load [N]	Life [cycles]
3	300	5.00	5890.49	2.00E+06
4	400	4.99	7822.60	2.00E+06
5	500	4.99	9778.25	958423
6	450	4.99	8800.42	885444
7	550	4.99	10756.07	213838
8	450	4.99	8800.42	1468220
9	550	4.99	10756.07	258788
10	500	4.99	9778.25	629575

3.5.2 Strain-Controlled Testing

Constant strain amplitude axial fatigue tests were carried out on three specimens of IT180 and one specimen of D176 in order to obtain the cyclic stress-strain curve of the alloys. All the tests were fully reversed with the mean strain zero, except for one specimen of IT180 that was tested at a strain ratio of $R = 0$. In all cases the control variable was the total strain amplitude, even though some literature reports suggest the plastic strain as the measured variable. This was, however not available by the equipment used. The servo-hydraulic machine is controlled by a computer, where a control program allows applying the desired loading during the tests through a sinusoidal wave. The parameter introduced to the control program is the longitudinal deformation of the gauge (in mm), so the desired strain amplitude should be calculated and entered in terms of this parameter. During the length of the test data of

the applied load together with the longitudinal deformation was stored in a file in the computer. Each specimen was aligned as for the stress-controlled and tensile tests. The contacting extensometer had a gauge length of 12.5mm.

Creation of the strain program:

Since the amount of specimens available was small, and for the sake of the simplicity, the method chosen for the estimation of CSS curves was the multiple step strain test. A set of blocks was created, each of them having a triangular loading waveform with constant strain amplitude, which was increased at every new block. The initial straining direction was tensile in all tests.

Firstly, two specimens of IT180 were tested at displacements of $4.2 \cdot 10^{-3}$, $4.6 \cdot 10^{-3}$, $5.0 \cdot 10^{-3}$, $5.4 \cdot 10^{-3}$, $5.8 \cdot 10^{-3}$, $6.2 \cdot 10^{-3}$, $6.6 \cdot 10^{-3}$, $7.0 \cdot 10^{-3}$, $7.4 \cdot 10^{-3}$, and $7.8 \cdot 10^{-3}$mm. One specimen was tested at fully reversed loading and the other with R=0, both with a constant frequency of 0.2Hz and 5 cycles per block. It was observed that this displacement sequence gave strain in % that ranged only within the elastic part of the alloy response. Also it was noticed that using a constant strain rate was more convenient for the desired purpose than using a constant frequency, since similar experiments were found in literature reports using constant strain rate [17], [19-20]. Because of this the information obtained from these two tests was not considered very useful, and no further discussion of these data will be performed.

Thereby, for subsequent tests, the frequency at each block was changed in order to maintain a constant strain rate of 0.05mm/s, equal to that used in the tensile testing. In the case of IT180 the strain amplitudes programmed were 0.1, 0.2, 0.3, 0.4, 0.5%. Since the entry parameter for the program was the gage elongation in [mm], the correspondent elongation amplitude was calculated based on the extensometer length to provide the % desired. For example, an elongation of 0.0125mm is equivalent to 0.1%.

The first fully reversed test consisted in 200 cycles per block. However, the specimen broke during the second block so the number of cycles for the next specimen tested was lowered to 30 cycles. Even so the specimen broke again at the second block. In the

case of D176 the strain amplitude sequence was 0.2, 0.3, 0.4, 0.5, 0.6, 0.7, 0.8, 0.9, and 1%. Even when complete separation of the sample did not occur, a crack on the surface was visible when the test finished.

According to ASTM standard E606 [18] there are several failure criterions depending on the final use of the fatigue life information. In this sense, it was not of interest to cycle the specimen until complete separation occurred, so the existence of a surface microcrack was enough to consider the specimen as failed. Table 3.8 below summarizes the strain amplitudes together with their corresponding frequencies for the last three specimens for both alloys.

Table 3.8 Cyclic frequencies at each strain amplitude. Note that IT180 was tested at strains between 0.1 and 0.5%. D176 was tested at all strains shown starting from 0.2%.

Strain amplitude [%]	Strain amplitude [mm]	Frequency [Hz]
0.1	0.0125	1.000
0.2	0.0250	0.500
0.3	0.0375	0.333
0.4	0.0500	0.250
0.5	0.0625	0.200
0.6	0.0750	0.167
0.7	0.0875	0.143
0.8	0.1000	0.125
0.9	0.1125	0.111
1.0	0.1250	0.100

Chapter 4 Results and Discussion

4.1 Surface inspection

The valleys on a rough surface serve as stress concentrators and a possible place for the nucleation of a dominant crack. In order to reduce this effect as much as possible, the samples were ground and polished as explained in chapter 3. However, residual stresses arising from the mechanical treatments when superimposed with the applied fatigue loads might alter the mean level [11]. In this sense, residual stresses would be detrimental if tensile and favourable if compressive as explained in section 2. Yet it was decided to carry out the surface treatment with the thought that the effect on fatigue strength of a rough surface could be more detrimental that the possible residual stresses induced by the surface treatment. However, a heat treatment after the wanted surface is achieved could be recommended to release these residual stresses.

Porosity is a typical defect of materials produced by powder metallurgy processes, since the complete theoretical density is almost impossible to achieve after sintering. Inspection of the IT180 specimens with the optical microscope showed that every sample presented a considerable amount of pores and cracks of different sizes and lengths, which could affect the fatigue response of the material. The largest pore registered had a length of 280µm and was found on specimen #4. Pores larger than 100µm diameter are considered dangerous and potential causes of future crack growth, and thereby a register of the approximate localization of such defects is relevant in order to later compare if the failures of the specimens relate to these pores.

Following, in figures 4.1 and 4.2, are two pictures of the same area of specimen #2, before and after grinding and polishing, taken at x100 magnification. Note also the diminishing of the roughness of the surface. During final inspection in the microscope it could be observed that pores and cracks of significant magnitude (more than 100µm length) kept more or less the same dimensions and shapes. However, there are some areas where the pores were eliminated while appearance of new pores was seen in other areas. In some places, small pores joined together to form a bigger one. Since there is no specific pattern in the presence, absence or shape of the porosity, it is

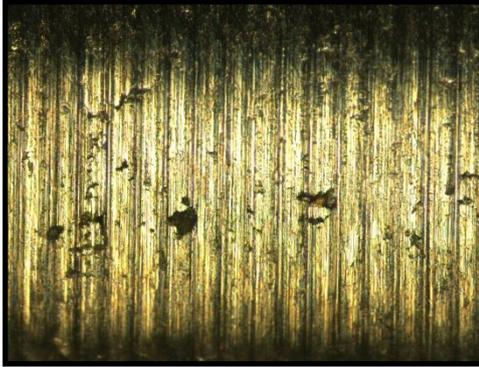thought that this defect is present throughout the material and is a defect that cannot be eliminated.

Figure 4.1 Specific area before grinding and polishing.
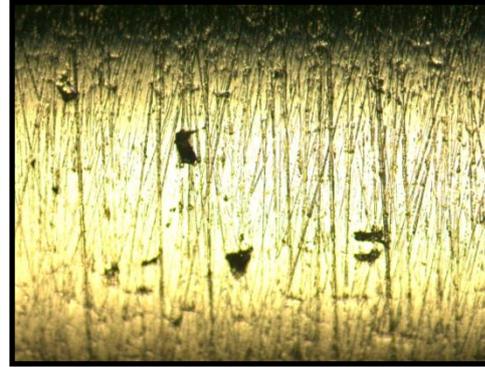

Figure 4.2 Same area as Figure 4.1 after grinding and polishing.

It is known that pores on free surfaces are likely to act as crack initiation sites. However, they are not necessarily the only causes for crack initiation since defects present within the material also can induce failure, and these defects cannot be registered or inspected prior testing.

Chawla et al. [26], [27], on their work with powder metallurgy steels used a pore shape form factor established by DeHoff to characterize the porosity of the material. Following the Shape Factor, F, formula is shown:

$$F = \frac{4 \cdot \pi \cdot A}{P^2}$$
(4.1)

where A is the area of the pore, and P its perimeter.

As some samples were exhaustively observed with an optical microscope at x100 magnification, all the pores larger than 100µm were registered with their position and size. It was decided to use the same F to characterize pore shape as Chawla et al. in this work, so the area and perimeter of the pores were measured and the irregularity of pores was estimated. The result can be seen in figure 4.3. Values of F near to one represent a nearly spherical pore shape while values tending to zero are pores completely irregular. As shown in figure 4.3 the bigger pores presented a lower shape factor whereas the smaller ones had a higher shape factor, indicating a more regular and near to round shape.
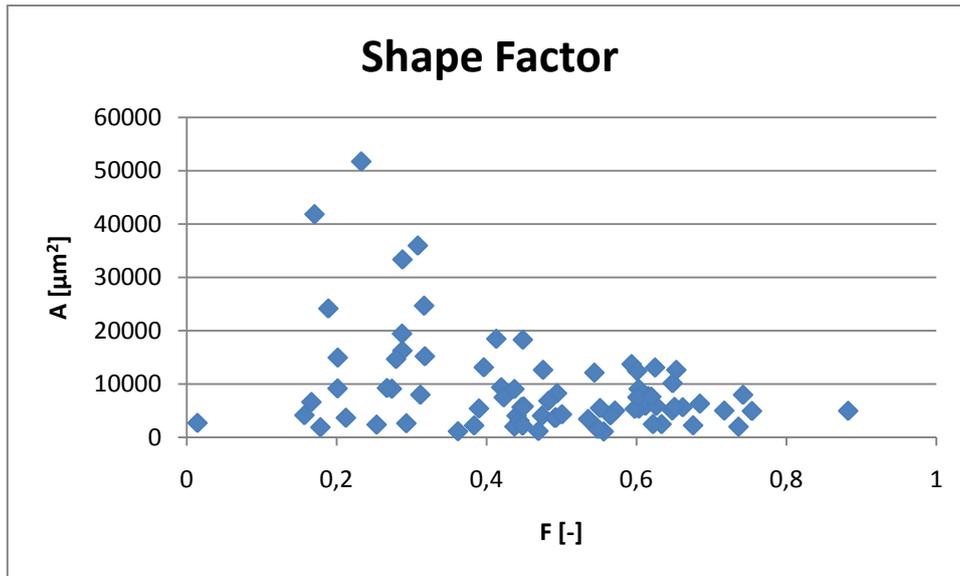
Figure 4.3 Shape factor calculated for the pores registered in 3 specimens of IT180.

On the other hand, while crack initiation in powder metallurgy materials is associated with the size and shape of the pores, the mean pore spacing is the principal factor that affects crack propagation rate. When pores are near each other the crack will propagate faster because it needs to travel a shorter distance before finding another pore, which instantly will increase the crack length and promote continued propagation. Due to the higher volume of porosity in IT180 the material had more zones with clusters of pores instead of isolated pores like in D176. However, in materials with a high density but yet a certain amount of porosity the presence of pores act as a delay or deviation for cracks, reducing the crack speed at crack propagation because, in this case, pores represent a discontinuity in the material, making the path for the crack more tortuous.

Also, it was observed that the porosity on the specimen surfaces was not uniformly distributed, i.e., there was more concentration of pores near the ends of the samples necks, where fractures have taken place, indicating that failure might have been related to porosity localized in that zone. Following figures 4.4-4.6 show where the pores were observed in 3 different specimens of IT180, the 3 with most pores detected. In the case of specimens #1 and #4, failure took place at the lengths 31mm and 38mm, respectively, where there was a considerably high pore concentration. Five

more specimens also broke in a zone that presented a higher number of pores. However, in the case of specimen #12 the bigger pores were not located where the fracture occurred (at 60mm). Despite this, it is thought that effectively porosity was a potential cause of fracture initiation in this sample. Note also that the rest of the porosity was uniformly distributed along the testing area.
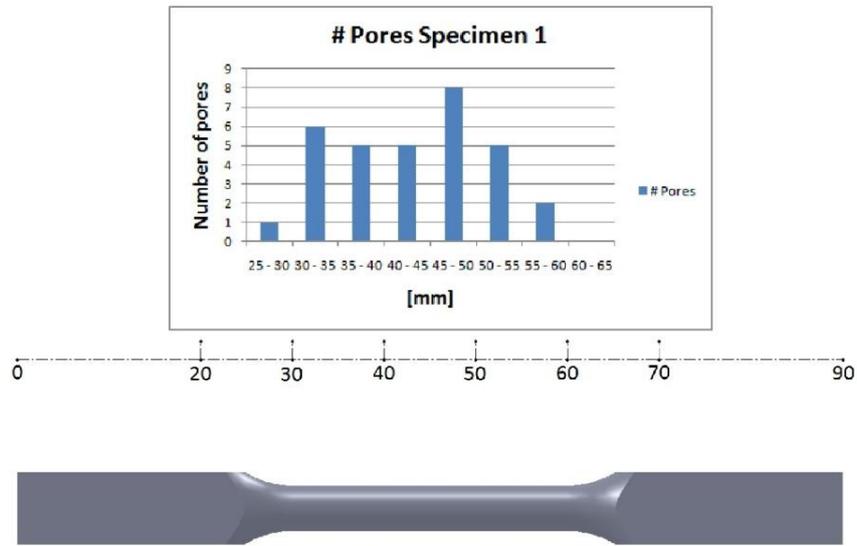

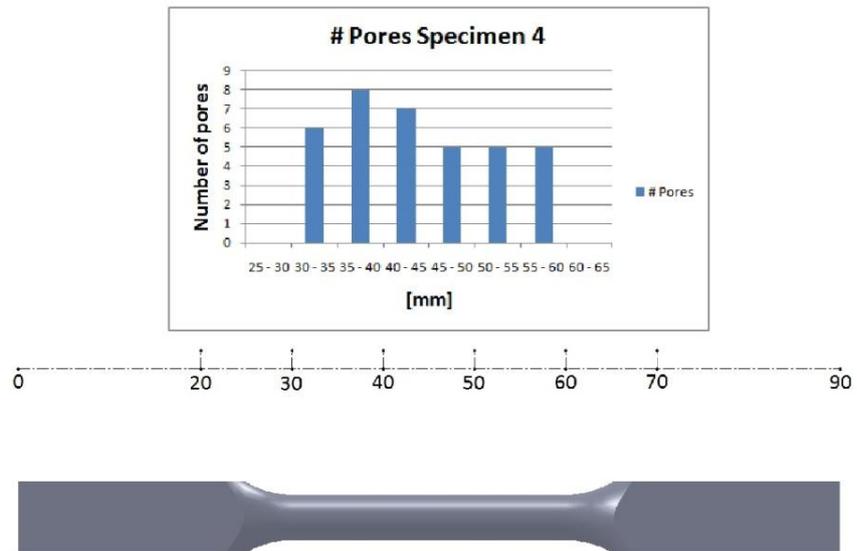**Figure 4.4** Pore distribution along specimen #1.

Figure 4.5 Pore distribution along specimen #4.
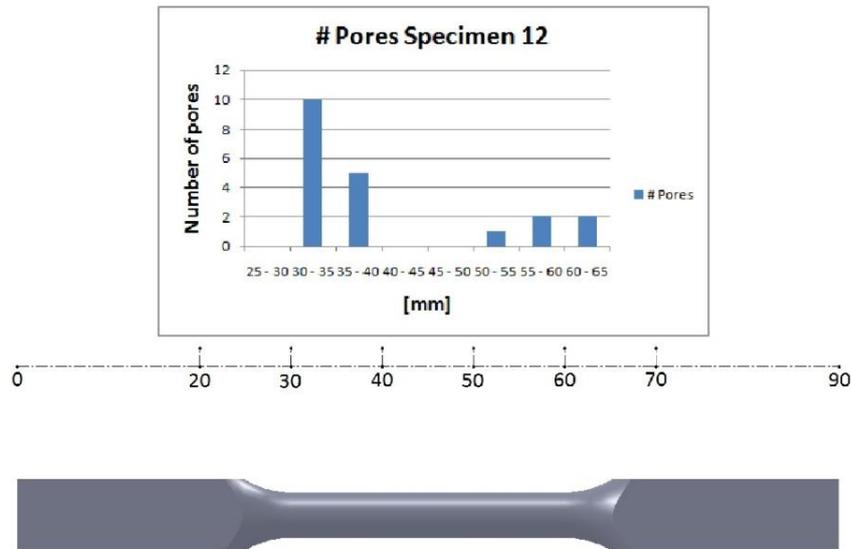
Figure 4.6 Pore distribution along specimen #12.

4.2 FEM Analysis

A Finite Element Method (FEM) analysis has been carried out in order to find out how the specimen geometry affects to the rupture pattern. The specimens used in this project have the same geometry for both alloys; the study was carried out with IT180 properties.

First of all, the sample geometry was modeled with the 3D CAD software SolidWorks, and afterwards analyzed and simulated using ABAQUS. The simulation consisted in applying pressure at two opposite sides at the top of the specimen, perpendicular to the faces, simulating the pressure made by the grips of the machine, and then a distributed shear force at the same faces, simulating the pulling force applied by the testing machine. The specimen is fixed at the other end. In this simple way, the stress distribution will be obtained, and give a good clue for designing new specimens for future studies.

The first analysis was done using a model with exactly the specimen size and dimensions, applying a 10kN force on the top of the specimen, distributed at two opposite sides, simulating the force transferred from the grips. This force magnitude was chosen because it is not high enough to make the specimen fail, but enough to create considerable stresses in the specimen. As the aim is to see where the stresses

are concentrated, the force value chosen is good for this purpose. Most part of the meshing was done using hexahedral elements, while the two neck regions were meshed using tetrahedral elements because of the complicated geometry. Once the meshing was done, the simulation was performed and the result is seen in figure 4.7.
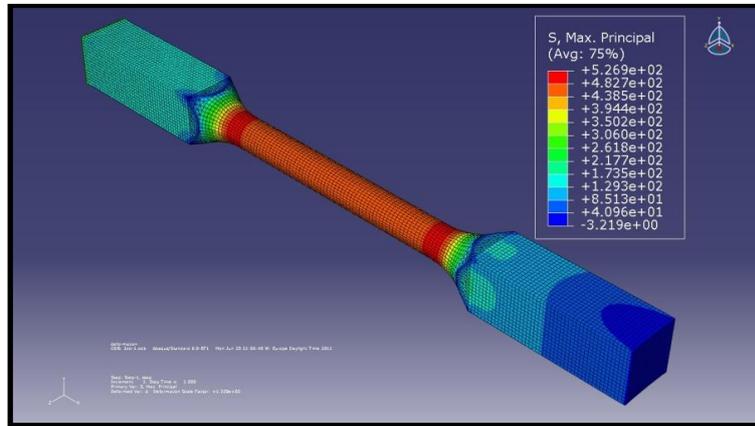
Figure 4.7 First analysis of specimen stress distribution to the real size model.

The scope of the simulation was to find the maximum principal stress value and its location, as assumed responsible of sample failure, and to be able to study its variation when slightly modifying the specimen geometry. After obtaining the real sample size simulation (figure 4.7), the radii from the grips to the necks (blend radii) were modified, making them larger and smaller, to see how this affects the stress distribution. Three more analyses were done for samples with different radii, see below in figures 4.8, 4.9 and 4.10.
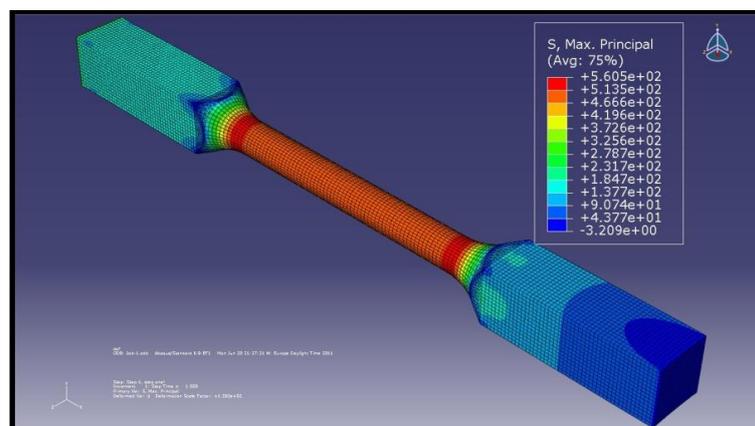
Figure 4.8 Second FEM analysis, with 8 mm radius model.
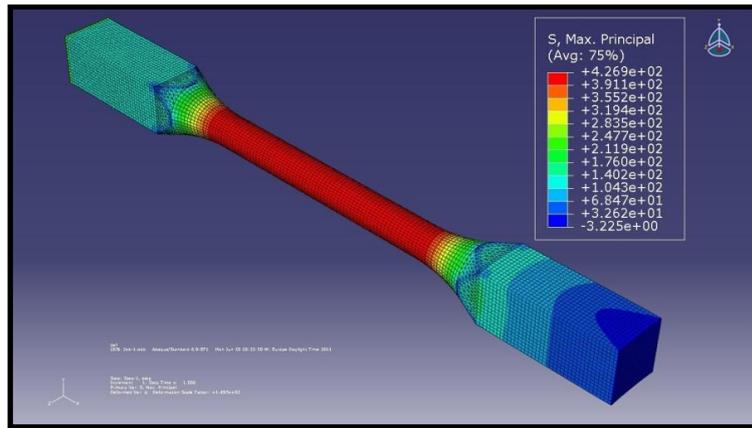
Figure 4.9 Third FEM analysis, with 20 mm radius model.
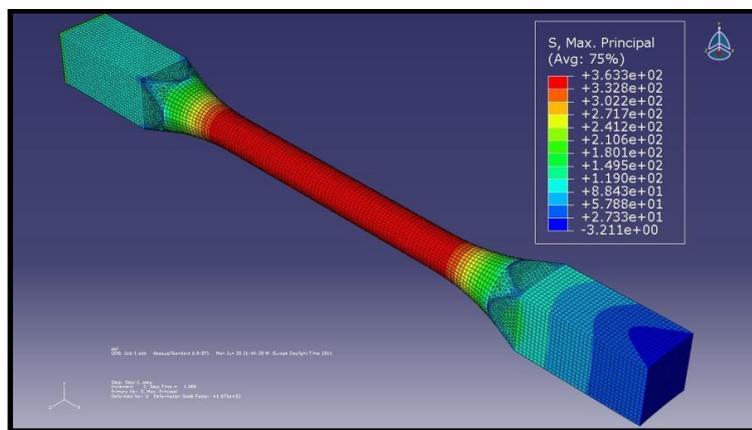
Figure 4.10 Fourth FEM analysis, with 30 mm radius model.

4.2.4 FEM Results

The FEM analyses showed interesting results about the stress distribution in the specimen. The first simulation, with the actual sample dimensions, showed a value of 526.9MPa of maximum principal stress in the sample. It is important to know this value to compare it with the following analyses with different radii, to see how much better or worse it is when modifying this critical parameter. Another field of study is where the stress concentrations occur, because the other goal of the FEM study is to try to distribute the maximum principal stress along the sample neck, and not concentrate it in the neck ends. Because of this fact, in the other analyses the neck ends radii were modified, making them both larger and smaller, to observe how the specimen behaves with such soft changes. As sharp corners and sudden cross-sectional area changes should be avoided not to concentrate stresses, the radius should be larger, but the contrary case was also studied to prove this argument.

In the second analysis, a model with 8mm of radius was studied (the real one is 10mm), and a higher maximum principal stress appeared in the same region as in the first simulation. The high stress is still present at the ends of the necks, as in the first simulation. Then, a third analysis was performed, in this case with a specimen with 20mm of radius, which showed that the maximum principal stress was lower than in the first and second analyses, and the stresses were also more uniformly distributed along the neck, thus not that concentrated at the sides. Finally, a fourth simulation was performed, modeling the specimen with 30mm radius, and in this case the maximum principal stress was lowered, and the tensions were more distributed along the neck. Table 4.1 shows the numerical results obtained from the simulations:

Table 4.1 The radius of the different models created and the maximum principal stress appearing in the model.

Radius [mm]	8	10	20	30
Max. Principal Stress [MPa]	560.5	526.9	426.9	363.3

The stress concentration factor K_t (Eq. 2.37) can be calculated, calculating first σ_{avg}, cf. Table 4.2.

$$\sigma_{avg} = \frac{F}{A_{neck}} = \frac{F}{\frac{\pi}{4}(d^2)} = \frac{4 \cdot 10000}{\pi 5^2} = 509.31 \ MPa$$

Table 4.2 Radius of the different models created, the maximum principal stress and the concentration factor K_t in each case.

Radius [mm]	8	10	20	30
Max. Principal Stress [MPa]	560.5	526.9	426.9	363.3
K_t [-]	1.10	1.03	0.84	0.71

It is clear that when increasing the radius, the maximum principal stress is decreasing. Increasing the radius makes the cross-sectional area change softly, so the stresses are distributed along the specimen necks, making this part of the geometry not so likely to be responsible of specimen failure.

Observing the K_t value for the models with a blend radius of 20 and 30mm it becomes lower than 1. It could be due to the stress distribution, so maybe the shear stresses were larger in those cases, so the shear stresses were also analyzed for the first model. The 20 and 30mm blend radii models show lower shear stresses and maximum shear stress levels as well, so it seems that all the shear stress components are lowered when the blend radius is increased. Following, figures 4.11, 4.12 and 4.13 show the shear stress components for the first model. The shear stress concentrations might also affect the fracture behavior.
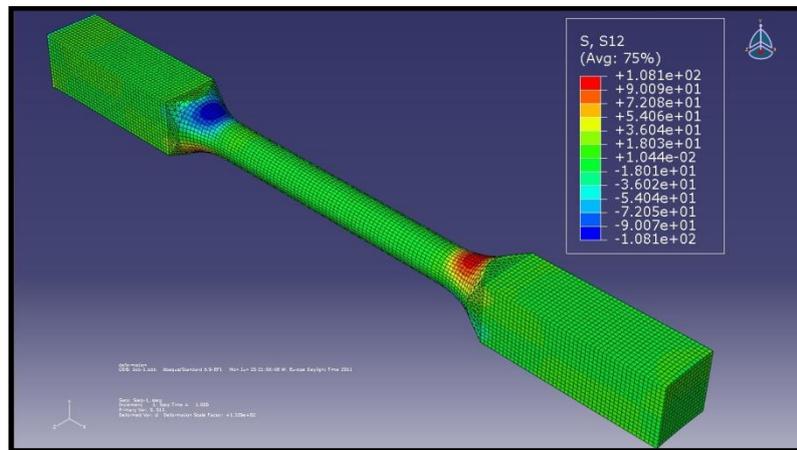

Figure 4.11 FEM analysis of the first model (10mm blend radius) showing shear stresses S_{12}.
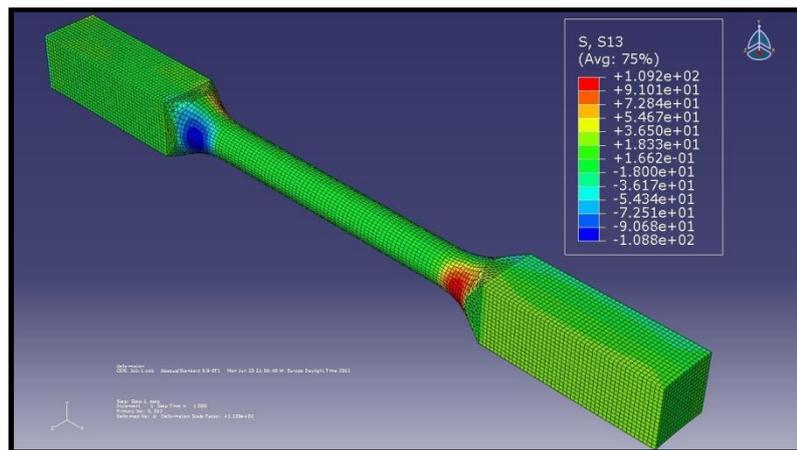
Figure 4.12 FEM analysis of the first model (10mm blend radius) showing shear stresses S_{13}.
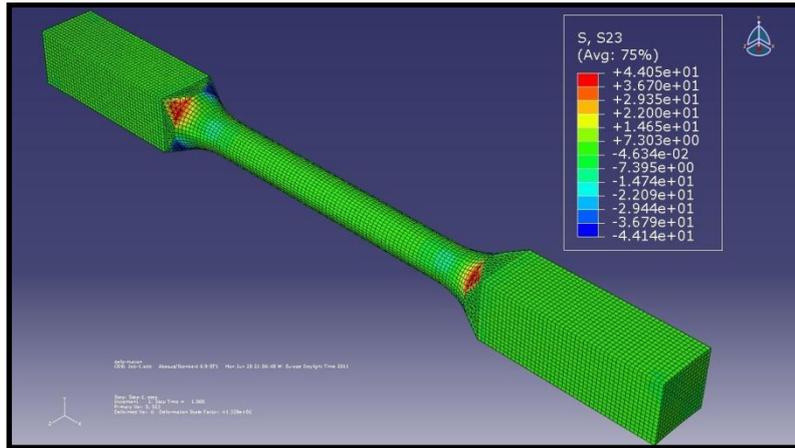
Figure 4.13 FEM analysis of the first model (10mm blend radius) showing shear stresses S_{23}.

4.3 Microstructural Examination

According to literature, both chemical composition and microstructural features are variables influencing the mechanical properties of tungsten heavy alloys. This is why, in order to provide a better comprehension of the fatigue behavior of Inermet 180 and Densimet 176, microstructural and fracture surface analyses were performed. The objective is to try to relate these analyses to the results obtained from the fatigue tests.

Figure 4.14 shows the microstructure of IT180 (W-3.5Ni-1.5wt%Cu) specimen #2 taken by scanning electron microscopy. In the picture the presence of tungsten grains, with an average diameter of 62μm, and a bonding phase between the grains can be distinguished. Dasa et al. [9] on their study of the microstructure and mechanical properties of tungsten heavy alloys worked with an alloy of the same composition as IT180 that presented tungsten grains of about 60μm diameter.

In general the W-grains are rounded in shape, but flattening of the grains is observed due to rearrangement during sintering. In the picture clear coarsening of tungsten grains is observed as also a considerable presence of W-W interface areas along with porosity trapped between grains. This porosity is also related to the sintering process.

Figure 4.15 shows the microstructure of Densimet 176. The average tungsten grain size of this alloy is 34μm. This alloy presents more rounded pores and less coarsening of

the tungsten grains. In general, W-Ni-Fe alloys present less W-W interface areas and smaller W grains than W-Ni-Cu alloys.

Figure 4.14 Microstructure of Inermet 180 alloy (SEM magn. x500).
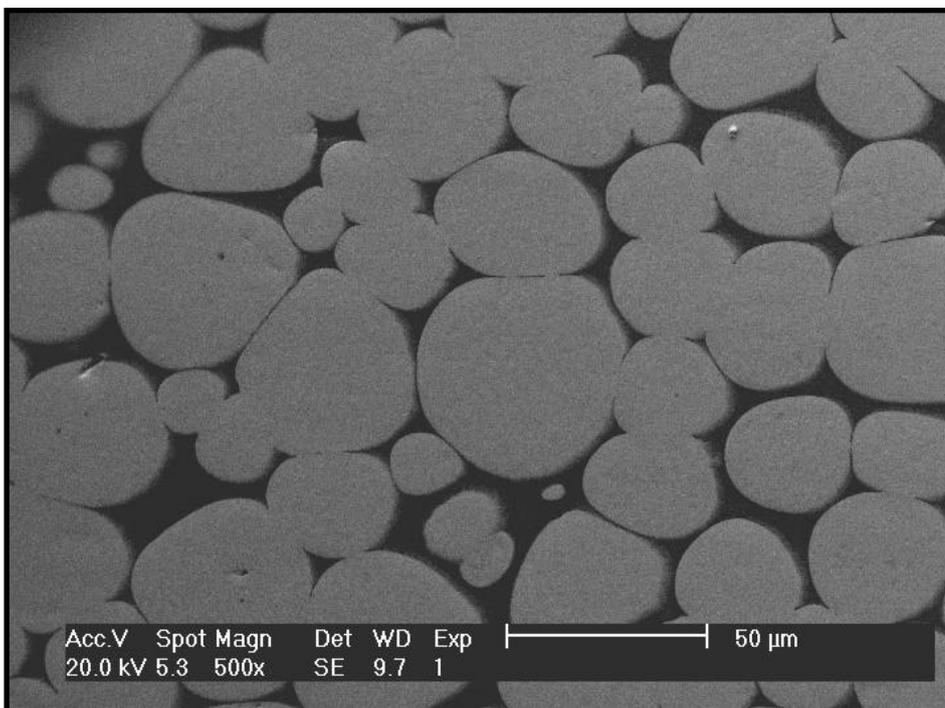
Figure 4.15 Microstructure of Densimet 176 alloy (SEM magn. x500).

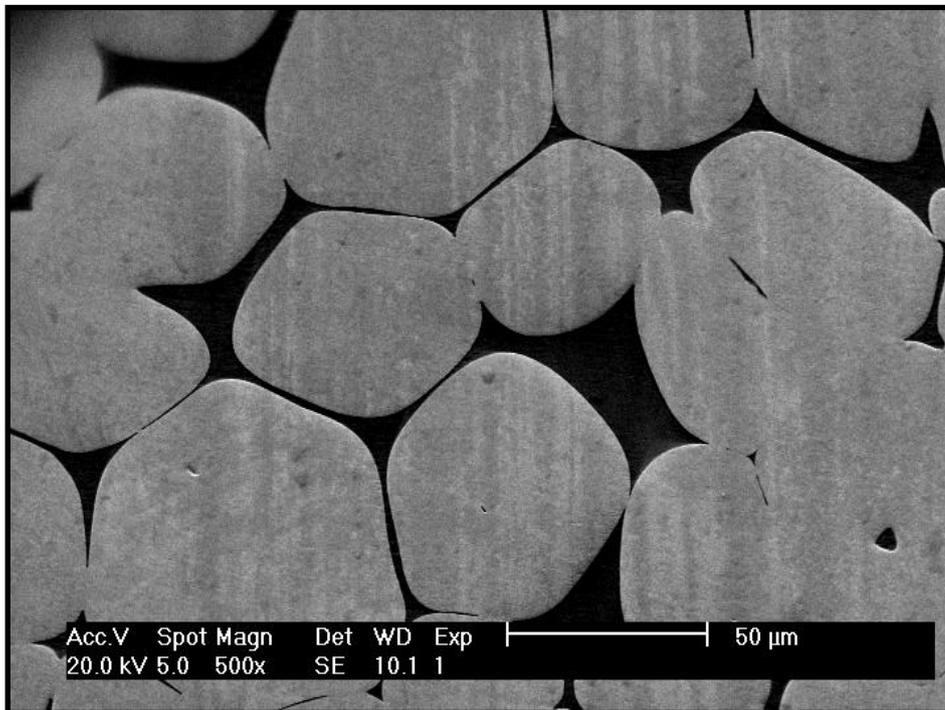The tungsten content is one of the main courses responsible for microstructural differences and subsequent change in mechanical properties between tungsten heavy alloys. Higher tungsten content requires higher sintering temperature that, at the same time, implies larger grains and further coarsening of them [9]. On the other hand, increasing the amount of tungsten decreases the amount of matrix and, consequently, the W-matrix interface areas [8]. There will then be less matrix phase located between W grains, in which case a higher amount of W-W interface areas will be present. This last feature, also known as contiguity, characterizes the amount of W-W interface area in proportion to the total interface area and is another important feature that affects, most of all, the ductility of these alloys.

X-ray mapping of the microstructure of IT180 showed the presence of the alloying elements nickel and copper mainly in the ductile bonding phase, see figure 4.16 below. The small presence of Ni and Cu within the grain areas could be particles removed by polishing during the preparation of the specimens and not completely taken away during cleaning. The X-ray mapping of the D176 microstructure shows presence of the alloying elements nickel and iron in the bonding phase, see figure 4.17. From a quantitative point of view a spot analysis of the compositions of both alloys show that the matrix of D176 is richer in tungsten (~50 wt%) as compared to that of IT180 (~30wt%), see figure 4.18 and Table 4.3. Furthermore, in the case of D176, the amount of nickel is very low compared to the amount of iron, something that was not expected since, theoretically, the nickel contribution should be higher than that of the other two components in the matrix. The composition is shown in Table 4.3.
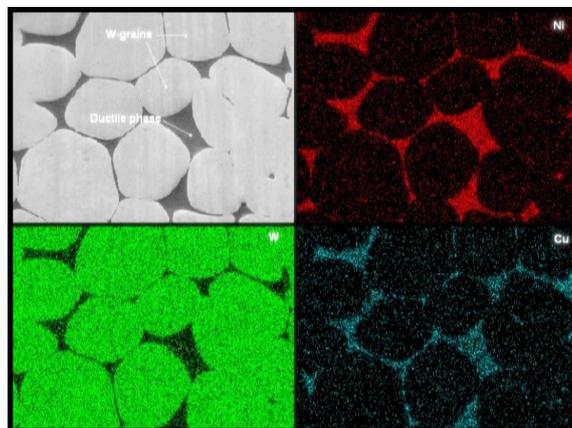
Figure 4.16 X-ray mapping by electron dispersive microscopy of IT180.
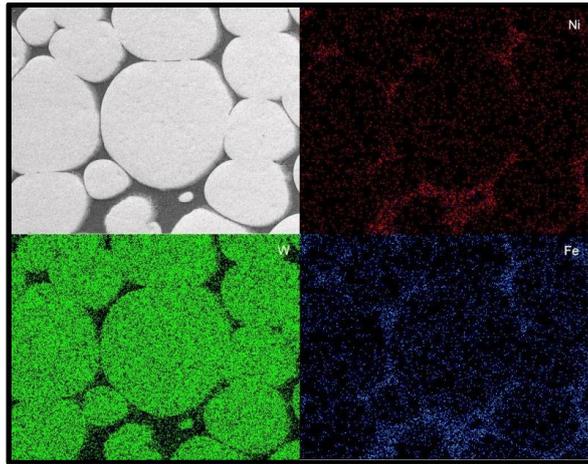
Figure 4.17 X-ray mapping by electron dispersive microscopy of D176.
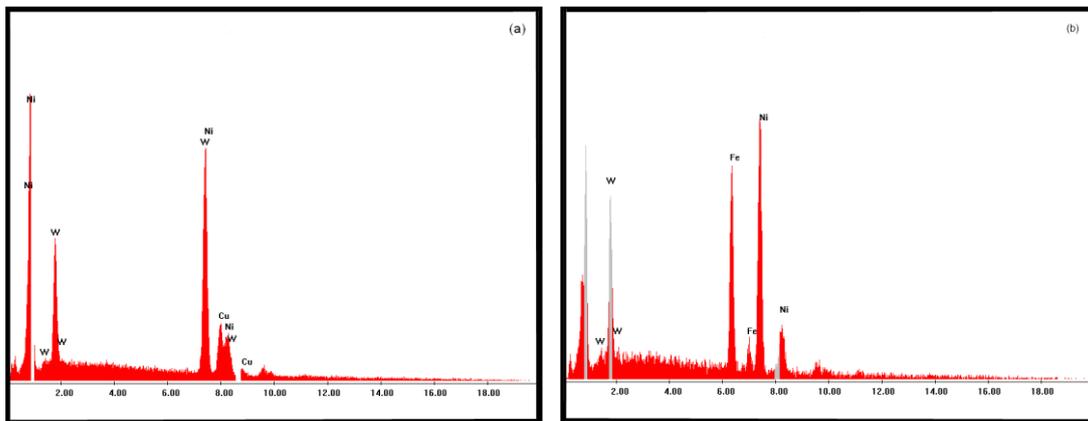
Figure 4.18 Composition analyses in a spot within the ductile phase of each alloy showing (a) Amount of nickel, copper and tungsten in the IT180 matrix and (b) Amount of nickel, iron and tungsten in the D176 matrix. ; Note the high presence of W in the ductile phase of D176.

Table 4.3 Spot analysis (wt%) of the matrix phase of the alloys.

Alloy	W	Ni	Cu	Fe
IT180	33.34	47.12	19.54	
IT180	30.66	50.77	18.57	
D176	51.38	16.39		32.23
D176	50.77	17.32		31.91

4.4 Tensile test

Two specimens of each alloy were tested under tensile loading. Information about the mechanical properties of both IT180 and D176 was provided by Plansee. However, it was considered necessary to characterize the same parameters at the laboratory at

LTH using the equipment that would be further used for the fatigue testing. Also, the samples to be tested were not in the same condition as when received, since surface grinding and polishing were performed. Table 4.4 summarizes all the results obtained along with the data from Plansee. Figures 4.19 and 4.20 show the recorded stress-strain curves.

Unfortunately, the first test run for IT180 did not provide reliable information because of the stop and later continuation of the test. The percentage of elongation to failure was 0.3%, which differs from the theoretical value (3%). Strengthening of the material is supposed to have occurred during the first part of this test. The gage length used was 12.5mm.

As it can be seen from Table 4.4, Inermet 180 shows a significant reduction in ultimate tensile strength (UTS), Young´s modulus and, especially, in percentage of elongation to fracture as compared to the as-received data. The variability between the two data sets is sufficiently large to be ascribed to experimental error or different testing conditions. Furthermore, the decrease of these properties can be due to the significant amount of porosity present in the alloys received at LTH that may not have been present in those tested by the company. In the case of the Densimet 176, an enhancement on the strengths is observed that may have been induced by cold working while grinding and polishing of the specimens.

Table 4.4 Tensile properties of IT180 and D176 provided by Plansee and obtained at LTH laboratory after surface machining.

	IT180		D176	
	LTH	**Plansee**	**LTH**	**Plansee**
Yield strength (offset = 0.2%) [MPa]	612	610	654	620
Ultimate tensile strength [MPa]	631	685	945	880
Fracture elongation [%]	0.6	3	42	20
Young´s modulus [GPa]	308	360	309	360

Porosity produced during densification can reduce the mechanical properties of these alloys. Under monotonic tensile loading, porosity reduces the effective load carrying cross-sectional area and acts as stress concentration sites for strain localization and damage, decreasing both strength and ductility [26]. Small and spherical pores seem to

have little effect on the properties whereas larger pores, formed during coalescence or gas evolution in over sintered specimens, sharply reduce the properties, specially the ductility [26].

This would be confirmed through the results for D176 that had just small, rounded and almost isolated porosity within the material. However, the enhancement gained with the cold work would be overcome by the porosity effect on IT180.

The strength and ductility are controlled by the amount of "load-carrying" cross-sectional area, i.e. the cross-sectional area of the material that contains no pores [27]. Thus, a high density material will have a larger deformed volume, which results in much higher ductility than a material with interconnected porosity, where deformation is more localized and the macroscopic ductility is lowered.

Comparing the properties between the two alloys, it can be noticed that there is none or almost no difference in the elastic behaviour between them, having similar yield strengths of 615MPa for IT180 and 650MPa for D176. However, a comparison between the ultimate tensile strengths and percentages of elongation shows a significant difference. This is explained by the higher amount of tungsten contained in D176. The ductility of WHAs is very sensitive to the tungsten content of the material, increasing with an increase of W. However, an increase in tungsten content has no significant effect on the elastic behaviour of these alloys.
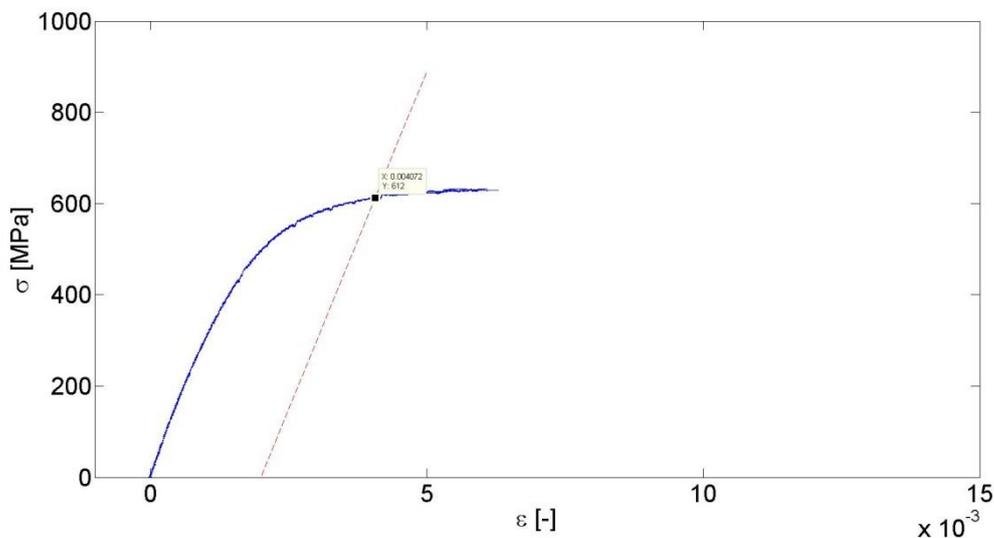
Figure 4.19 Stress vs. Strain diagrams of Inermet 180.
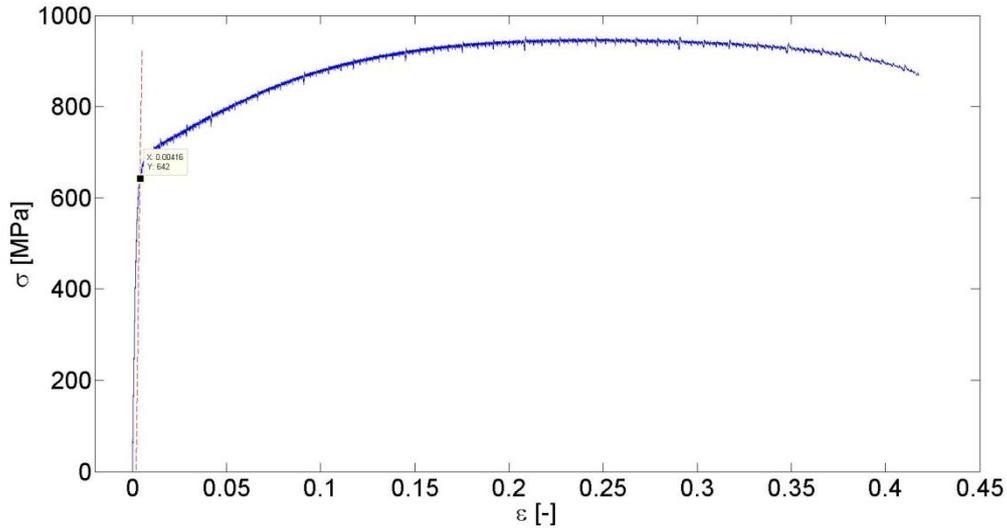
Figure 4.20 Stress vs. Strain diagrams of Densimet 176.

4.5 Fatigue results

4.5.1 Stress-Controlled Tests

The results obtained for IT180 and D176 are plotted on a log-log scale according to E739 Standard practice for Statistical analysis of linear or linearized Stress-Life (*S-N*) fatigue data. This practice aims at generating a statistical *S-N* curve in the finite fatigue life region, and therefore the samples tested at stress levels below the fatigue limit (which had infinite life) are not taken into account in these computations.

In the case of IT180, four stress levels were used: 300, 250, 225 and 210MPa and a total amount of specimens to perform the calculation equals 9, giving the percentage of replication equal to 55.6%.

The data for these stress levels was plotted on a log-log scale. Noting that the distribution of the points seemed to follow a straight line, computations to obtain the median curve were performed. In this sense, the estimators of A and B and the variance of the curve are, respectively:

$$\hat{A} = 26.783 \qquad\qquad \hat{B} = -8.967 \qquad\qquad \sigma = 0.268$$

Then, substituting these values in Eq. 2.11, the median curve would be:

$$Log(N) = 26.783 - 8.967 Log(S_a)$$

and expressing it in the form of the Basquin equation Eq. 2.6:

$$S_a = 1048(2N)^{-0.112}$$

where the fatigue coefficient and exponent are $S'_f = 1048 \text{MPa}$ and $b = -0.112$, respectively.

Finally the design curve with a reliability of 90% and a confidence of 95% was estimated. For this: $K_{OWEN} = 2.727$ and the design curve is:

$$Y = \hat{A} + \hat{B} \cdot X - K_{OWEN} \cdot \sigma \rightarrow Y = 26.783 - 8.967 LogX - 2.727 \cdot 0.268$$

or its equivalent version in a logarithmic scale:

$$S_{R90C95} = 868.318 \cdot (2N)^{-0.112}$$

For the case of the D176, 6 specimens were tested at 3 different stress levels that were 550, 500 and 450MPa (2 specimens at each level). Then the percentage of replication equals 50%.

In both cases IT180 and D176 the minimum number of specimens and the percentage of replication used are in accordance with the requirements suggested in E739-ASTM standard practice for conducting a preliminary and exploratory research and development fatigue testing.

Following the same procedure as used with IT180, the estimators for the statistical median *S-N* curve for D176 are:

$$\hat{A} = 26.790 \qquad\qquad \hat{B} = -7.791 \qquad\qquad \sigma = 0.153$$

Therefore the median *S-N* curve can be expressed as:

$$Log(N) = 26.790 - 7.791 Log(S_a)$$

and its equivalent version as the Basquin equation for the D176 would be:

$$S_a = 3000 \cdot N^{-0.128}$$

where the fatigue exponent and coefficient are $S'_f = 2744.47 \, MPa$ and $b = -0.128$, respectively.

Finally the design curve with a reliability of 90% and a confidence of 95% was estimated. For this $K_{OWEN} = 3.560$ and the design curve is:

$$Y = \hat{A} + \hat{B} \cdot X - K_{OWEN} \cdot \sigma \rightarrow Y = 26.790 - 7.791 \cdot X - 3.560 \cdot 0.153$$

or its equivalent version in a logarithmic scale:

$$S_{R90C95} = 2553 \cdot (2N)^{-0.128}$$

The computed curves together with the experimental data for both alloys are shown below in figures 4.21 and 4.22.
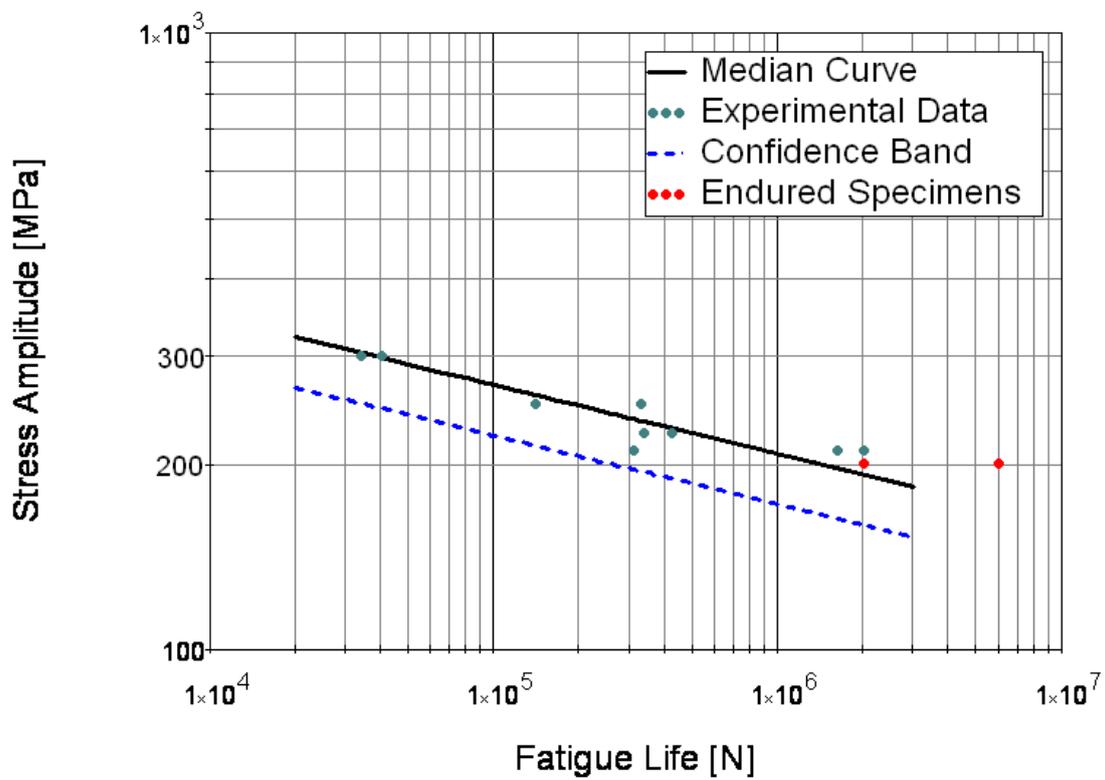
Figure 4.21 Experimental data of IT180 in the finite life region along with the statistical median curve and the confidence band.
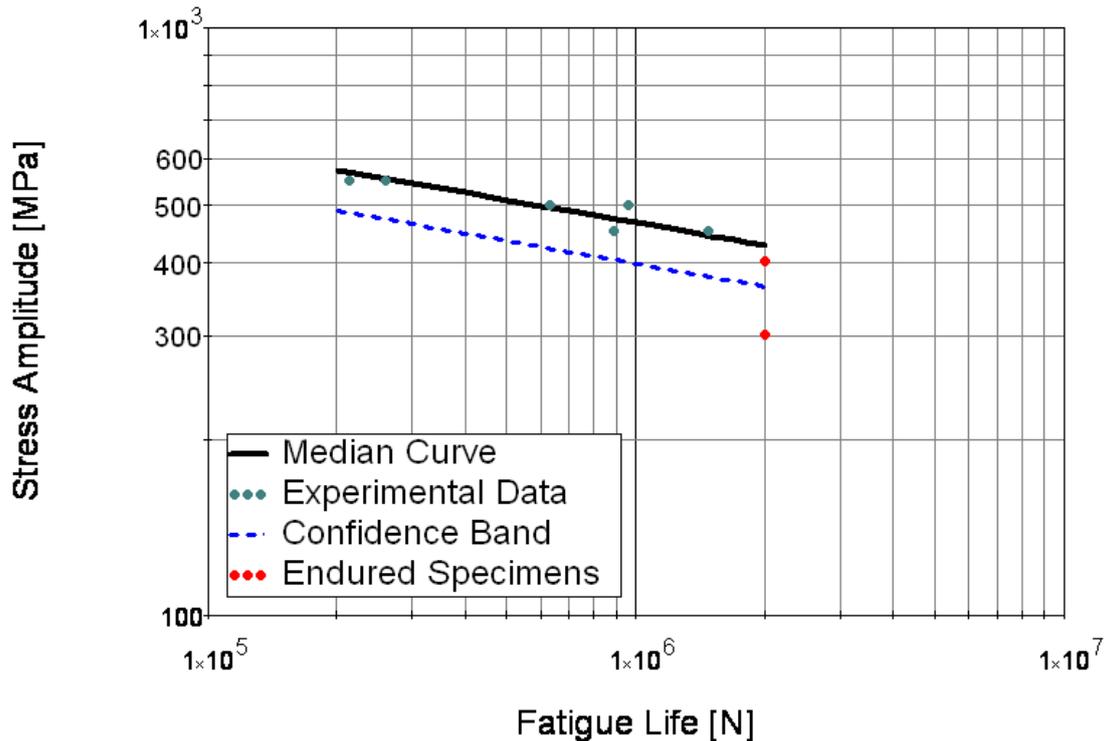
Figure 4.22 Experimental data of D176 in the finite life region along with the statistical median curve and the confidence band.

Comparing the results between IT180 and D176, the latter has higher fatigue strength, having higher number of cycles to failure, when subjected to the same stresses. On the other hand, the endurance limit for D176 is about 45% of its ultimate tensile strength whereas the endurance limit of IT180 only is about 33% of its ultimate tensile strength. This is in the lower region of the typical endurance limit values for most metals.

Since the number of samples usually is limited and, in our case very small, the distribution of the fatigue behaviour of the material is hard to predict exactly. Then 95% of confidence bands with 90% of reliability are drawn in the plots together with the median curves because if a series of analyses is performed with this material and design curves are computed for the corresponding data, 95% of the samples tested will have a 90% chance of survival at that stress.

Note that according to ASTM standard practice E739, the confidence band suggested is the double-sided hyperbolic confidence band. However, this practice also agrees on

the use of a linear one-sided lower bound as a confidence band. This is the procedure followed in this Thesis for sake of the simplicity of the calculations.

All specimens endured more than 10^4 cycles before failing, proving that they are definitely in a zone of relatively high cycle fatigue and, thereby, the study of the data was accurately obtained from load controlled constant amplitude tests and analysed using a stress-life approach.

Also, for the specific interval of stresses tested, the fatigue life can reasonably well be approximated to a straight line so that a mean *S-N* curve by ASTM standards can be obtained.

The values of the stress exponent for most metals range between -0.05 and -0.12 [11], which indicates that both our alloys are in the top limit of this range. On the other hand, S'_f can for most metals be approximated by the true fracture strength σ_f, corrected for necking, in a monotonic tension test [11]. This value would correspond to the intercept of the stress-life curve with the ordinate at one-quarter of the first cycle. In the present case the true fracture strength for IT180 and D176 are 633MPa and 1180MPa, respectively. In contrast, the fatigue strength coefficients for each alloy are 1048MPa and 3000MPa, respectively. Keeping in mind that, because the actual *S-N* relationship is approximated by a straight line only within a specific interval of stress and because the actual fatigue life distribution is unknown, it is not recommended that the *S-N* curve is extrapolated outside the interval of testing. Then the difference between the values of the true strength and the computed values of S'_f (especially for D176) indicate that it is not recommended to use the median curve obtained for extrapolation to lower fatigue lives. But the comparison between S'_f and σ_f is just an approximation and do not necessarily mean that these stresses have to be equal.

It is important to mention that one of the conditions for the statistical model proposed by E739 is that there are neither run-outs nor suspended tests for the entire interval of lives used in testing. However, specimen #10 of IT180 alloy did not fail even up to 2×10^6 cycles, and thereby it is considered as a run-out. Despite this fact we decided to still include this value in the calculations since there are other two more specimens at the same stress level (210MPa) that actually did fail.

Looking at the fatigue data plotted in figures 4.21 and 4.22 it is noticeable how the scatter between the lives obtained at each of the stress level increases the lower the stress levels are, in accordance to the literature.

Despite the fact that there is a large scatter in the fatigue data of the D176 alloy, the higher fatigue strength that this material presents compared to the IT180 alloy is easily observed. This can lead to the assumption that fatigue strength, and specially the endurance limit of a material, can be related to or determined by the ductility of it since the most noticeable difference between the present alloys lies on this aspect.

Finally, Morrows equation (Eq. 2.10) was used to see the influence of a mean stress of 30MPa on the fatigue curve and the results are shown in figures 4.23 and 4.24. It is easy to see how the median *S-N* curve for constant stress amplitude almost overlaps with the *S-N* modified by the mean stress. This shows that if we would have run the tests using a mean stress, the results would not have differed considerably (at least for the mean stress of interest).
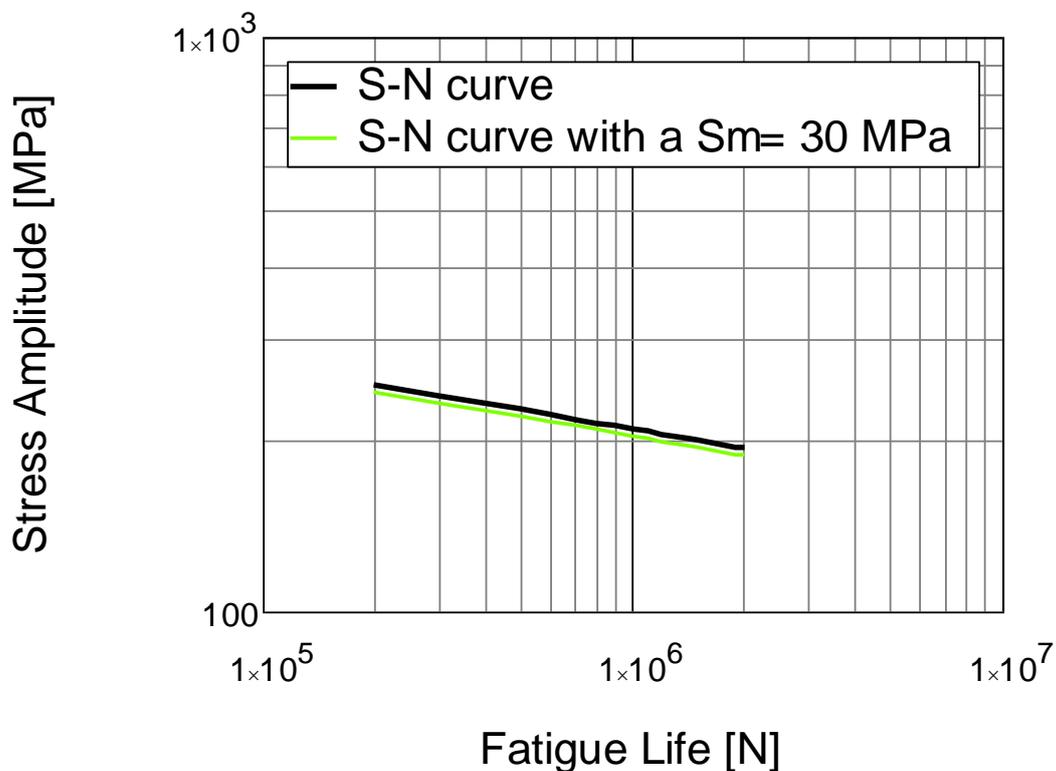
Figure 4.23 Mean stress effect in the *S-N* curve of IT180.
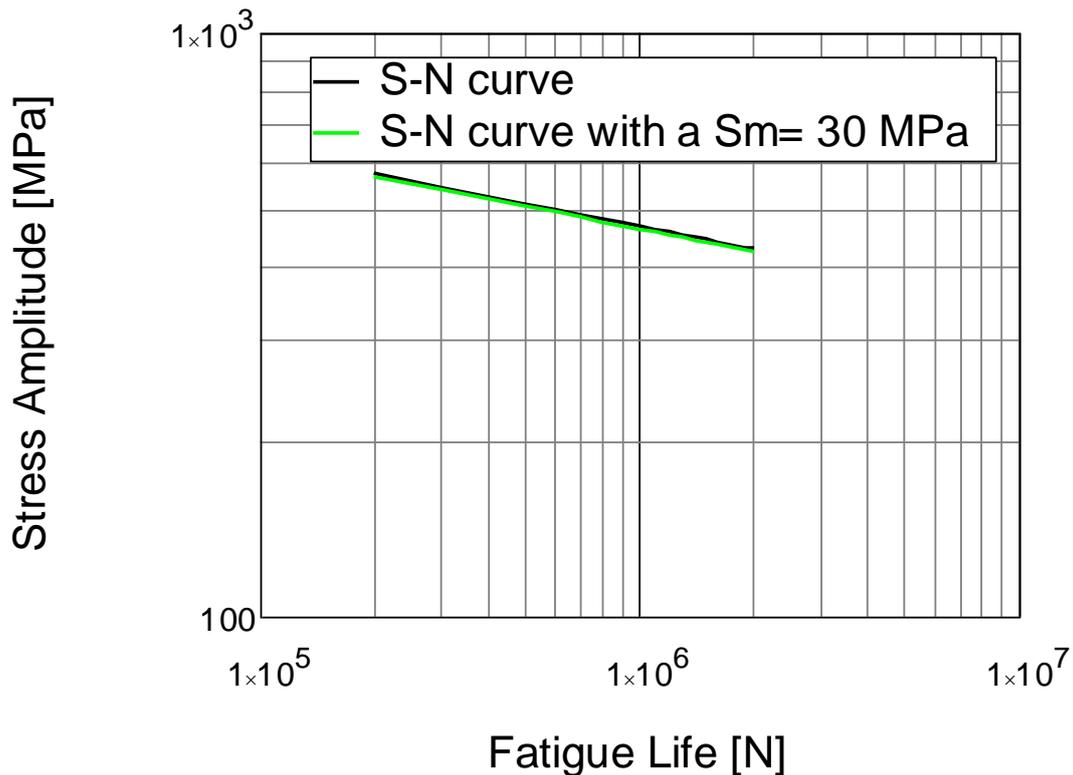
Figure 4.24 Mean stress effect in the *S-N* curve of D176.

The fracture surfaces were observed by scanning electron microscope and show the different fracture modes of both tungsten alloys, in fact related to their ductility and, therefore, to their fatigue strength.

In this sense the fracture mechanisms or modes of tungsten heavy alloys are a combination of intergranular W fractures, interfacial matrix-W decohesion, W transgranular cleavage and ductile rupture of the matrix. A graphical description of these mechanisms is shown in figure 4.25.

In general, low ductility alloys (shorter elongation to fracture) have a fracture surface where matrix-W debonding and intergranular decohesion of contiguous W grains predominate whereas an alloy with higher ductility have less presence of interfacial decohesion and a higher proportion of transgranular cleavage of W grains.

W-W interfaces are weak links in the microstructure and the easiest path for crack growth since these interfaces represent the lowest strength against fracture. The

reason is because the critical energy release rate is lowest for decohesion of these interfaces [28], [29].
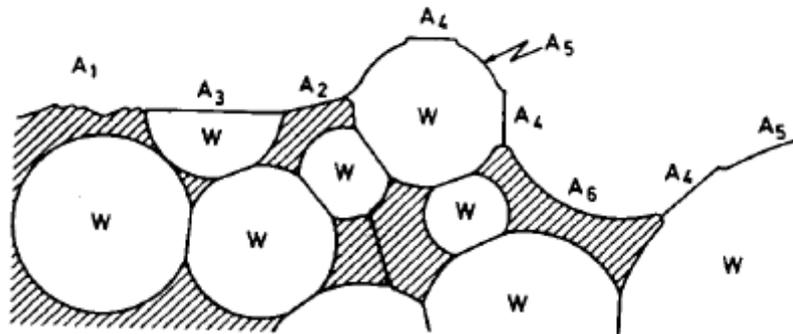
Figure 4.25 Schematic illustration of major failure modes. A1= ductile fracture of matrix-phase; A2= integranular fracture of matrix-phase; A3= transgranular cleavage; A4= intergranular fracture of W-grains network; A5= tungsten side of W-matrix interface fracture; A6= matrix side of W-matrix interface fracture. (Picture taken from reference [8].)

This is why alloys with a high contiguity have lower ductility; they have a large amount of low strength intergranular bondings that separate very easily, reducing the load which can be carried by the grains and, thus, decreasing their ductile properties.

On the other hand, Zamora et al. [28] points out that cracking of the W grains by cleavage needs good transmission of stresses from the matrix to the spherical or ellipsoidal grains through the interfaces so that, rather paradoxically, good interfacial bonding produces ductile alloys whose fracture surfaces show a maximum of cleavage.

From a microstructural point of view the difference between the present two alloys can be explained as follows. As it was mentioned before, higher tungsten content increases the final grain size, more coarsening of the W-grains is created and larger areas of W-W interface are preset. This is also enhanced by the lesser amount of bonding ductile phase to provide more W-matrix interfaces.

So, IT180 alloy that presents a lower ductility is expected to have a majority of W-matrix interface failure together with decohesion of tungsten grains. Figure 4.26 shows the fracture surface of this alloy, where tungsten grains have flattened areas due to

the separation between them and other tungsten grains. Also in the figure it can be noticed a crack growing through the matrix phase and continuing between this one and the W grain boundary.
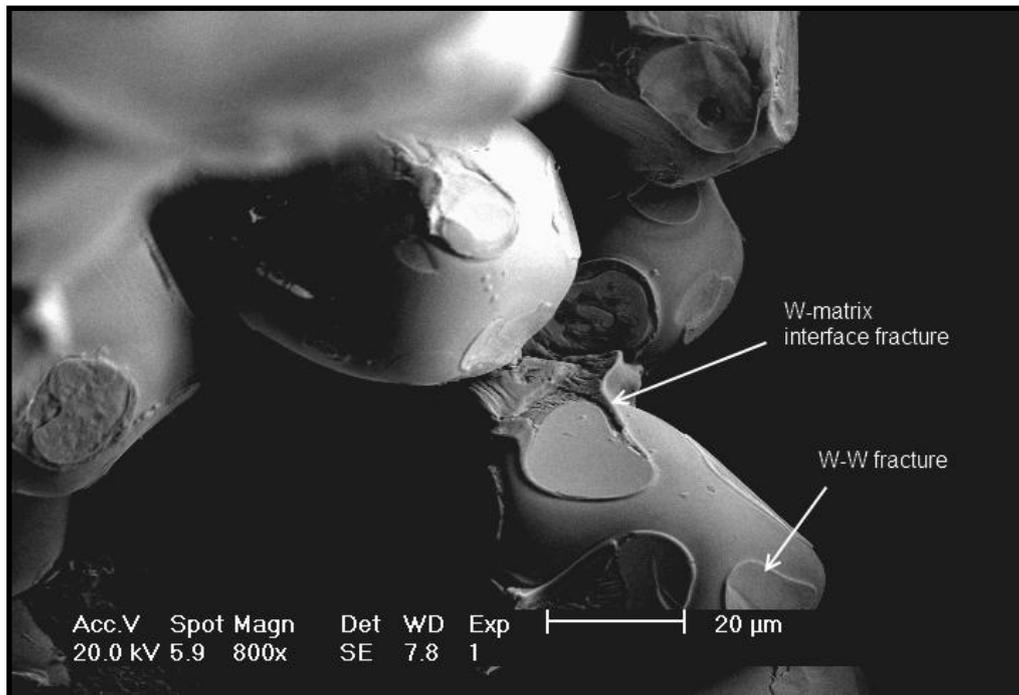
Figure 4.26 Fracture surface of IT180 at x800 magnification (SEM).

In the case of the Densimet 176 alloy, a combination of W-matrix failure and transgranular cleavage of tungsten grains can be observed in figure 4.27. Here it can be seen how cracks propagate between the grains boundaries and the ductile matrix and then go through the grains, giving them these radial striations that continue growing. Note that there is also the presence of smooth tungsten grain areas associated with an intergranular fracture mode, but this mechanism is overcome by the two latter ones. Cyclic stresses induce deformation in the material due to back and forth sliding on closely spaced parallel planes in a narrow band known as persistent slip bands. This deformation mode causes striations on the surface that accumulates progressively, concentrating the stress until a crack is formed. Once the crack is formed two scenarios can occur. If the crack is long enough it will propagate and cause part failure. Or the crack form but do not propagate, giving the chance to the formation of several other cracks that can cause failure. The stresses at the tip of the crack are very high

and might break the atomic bonds in the crack tip area, and the crack can increase in length.
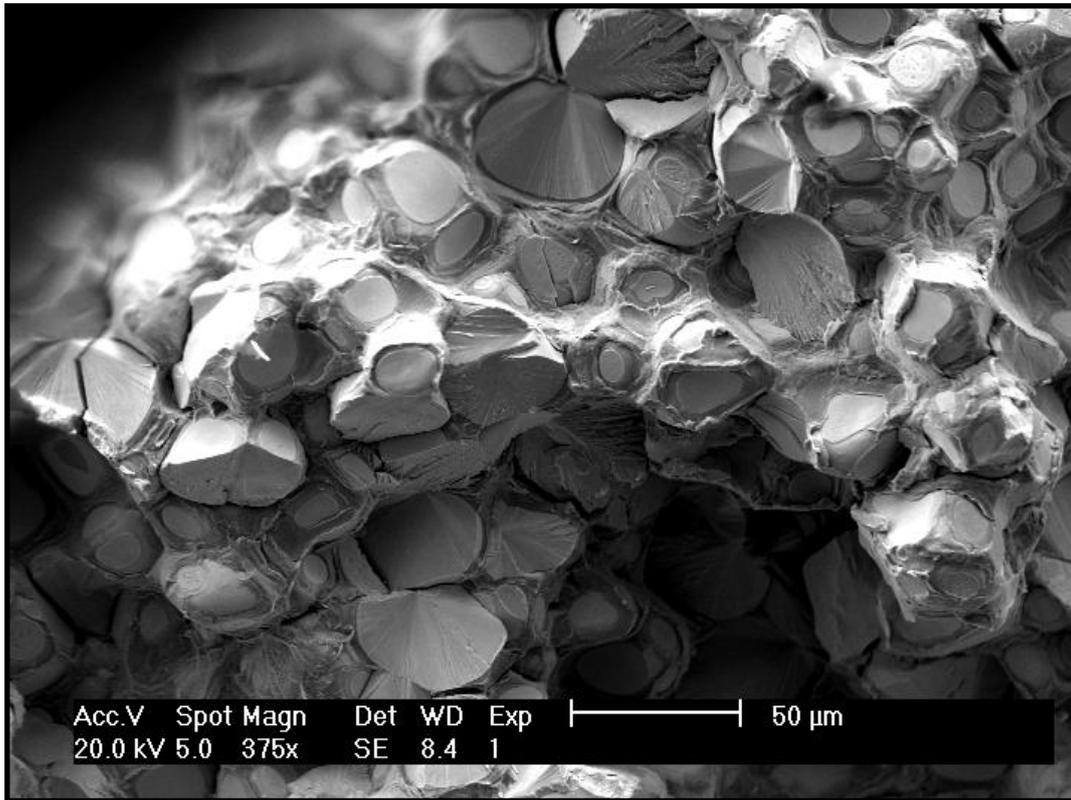
Figure 4.27 Fracture surface of D176 at x375 magnification (SEM).

4.5.2 Strain controlled tests

The specimen of IT180 tested with blocks containing 200 cycles broke at the second block at a strain amplitude of 0.2 % in 29th cycle. The specimen broke despite of the fact that the wave program was giving a strain in [mm] equivalent to the desired strain in [%]. That this was performed properly is shown by the fact that the strain amplitudes obtained were almost exactly the same as those programmed. For example, at 0.2% strain amplitude the peak strain was 0.193%.

Figure 4.28 shows the stress vs. strain amplitudes for this specimen. At 0.1% strain the behavior of the material is completely elastic and the specimen failed before yielding of the material. The reason why this material has failed so early could be due to poor alignment of the specimen. In this sense, ASTM standard practice E606 recommends

that the bending strains should not exceed 5% of the minimum strain amplitude, especially in testing of low ductility material such as IT180. The minimum strain amplitude was in this case equivalent to 0.0125mm, whereas the lateral displacement measured by the strain gages was in the order of magnitude 10^{-2}mm, which is much higher than 5%.

At a strain of 0.1% the specimen stabilizes after about 40 cycles, while at 0.2% stabilization takes place after 15 cycles with the tensile peak stress 519MPa. Comparing the results from the specimens tested with blocks of 200 or 30 cycles it was noticed that the stabilized peak stresses in tension are almost the same (with an approximate difference of 4MPa) whereas the difference in compression is more considerable (about 40MPa). In this respect, the specimen that was subjected to the initial 200 cycles reached higher stress amplitude at the next strain level, which can be because the material was able to harden more with the higher number of cycles.
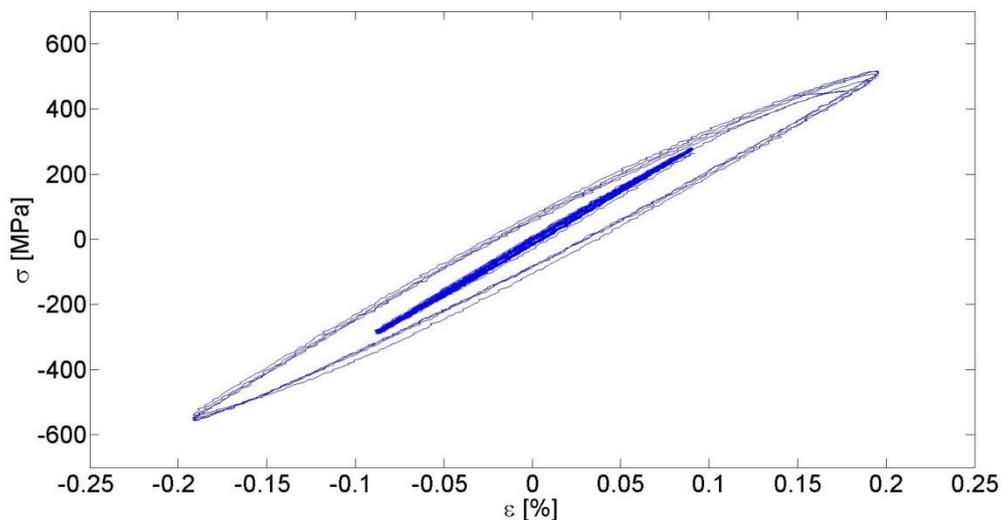
Figure 4.28 Hysteresis loops for IT180 until 0.2% of strain amplitude.

In the case of D176 the specimens were tested until a deformation of 1%. The resulting hysteresis loops are shown in figure 4.29. Figure 4.30 shows the variation of the stress amplitude with cycling in time for the entire test length. For initial strain amplitudes between 0.2-0.5%, cyclic hardening is more noticeable while the stress stabilizes at about the 20th cycle of each block. However, at higher strain amplitudes, up to 1%, the

stress amplitude variation at each cycle is very small and the obtained hysteresis loops are stabilized.
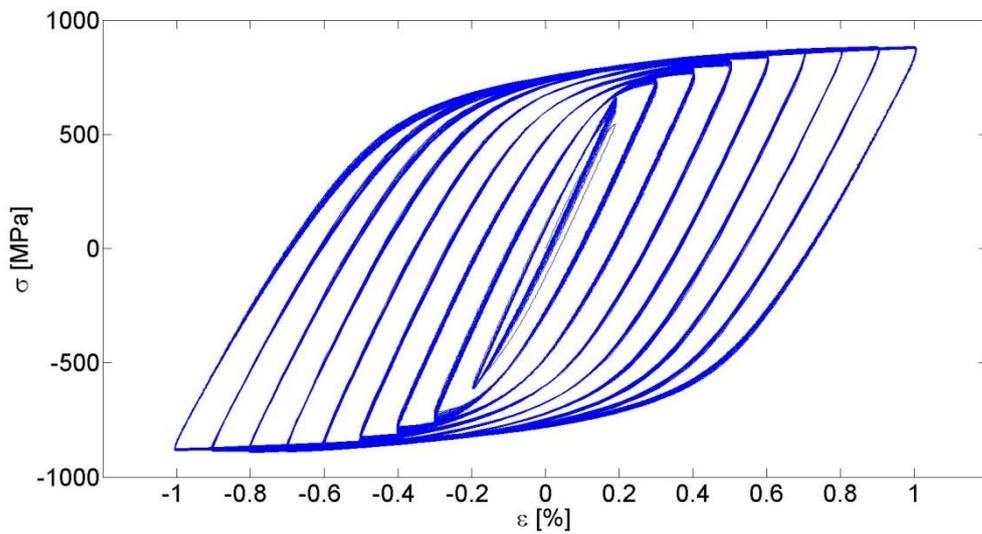
Figure 4.29 Hysteresis loops for D176 until 1% of strain amplitude.
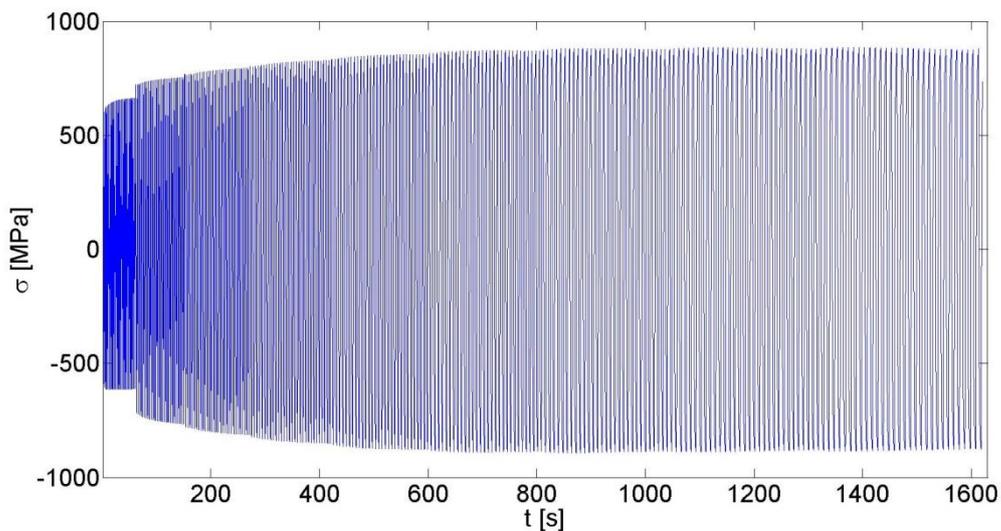
Figure 4.30 Variation of stress amplitudes at each block with time.

Cyclic vs. Monotonic response:

In order to compare the cyclic and monotonic behavior of the alloys, the tensile curves of IT180 and D176 are shown in figures 4.31 and 4.32 (red lines) superimposed on the tensile side of the hysteresis loops (first quadrant). The cyclic parameters K' and n'

where not estimated for IT180 since just a small part of the curve could be drawn. However, even when the fatigue test reached only within the elastic region, it can be observed that the cyclic curves lie above the monotonic curve and it is expected to have continued to follow this pattern if cycling would have continued. In this sense it may be said that IT180 hardens under cyclic loading.
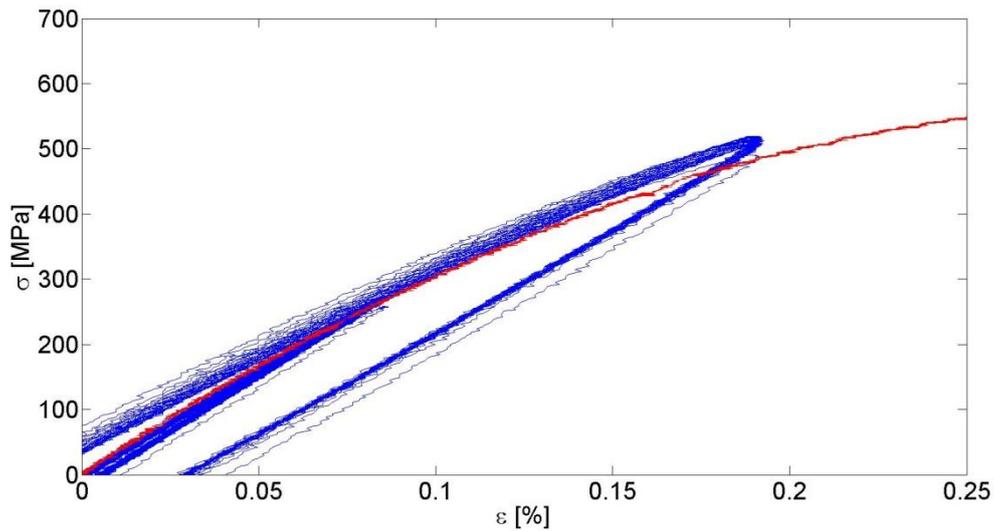
Figure 4.31 Tensile side of the hysteresis loops for IT180 together with the tensile stress-strain curve.
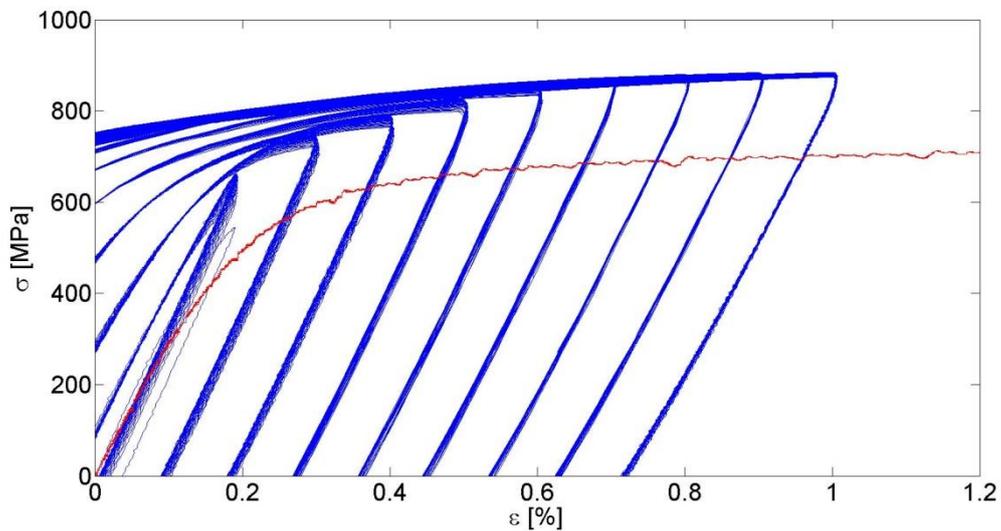
Figure 4.32 Tensile side of the hysteresis loops for D176 together with the tensile stress-strain curve.

The cyclic yield stress (S'_y) is the stress at 0.2% plastic strain on a cyclic stress–strain curve. In the case of D176 this value was determined as proposed in reference [13] by constructing a line parallel to the modulus of elasticity through the 0.2% strain offset

at zero stress level. The stress at which the line intersects the cyclic stress–strain curve is taken as the cyclic yield stress. The cyclic yield strength of D176 is about 800MPa, which is higher than the monotonic yield strength (654MPa). This indicates that D176 hardens under cyclic loading.

The cyclic parameters K' and n' were estimated and compared to the monotonic parameters K and n. The procedure was as follows:

The values of the stabilized stress amplitudes at the tip of the hysteresis loop for each strain amplitude were read from the cyclic stress-strain curve shown in figure 4.32. Then, the elastic and plastic strains were calculated by Eq. 2.31 and Eq. 2.32. These data are presented in Table 4.5.

Table 4.5 Stress and strain amplitudes extracted from the CSS curves used to estimate the cyclic strength coefficient and the cyclic strain hardening exponent. The calculated elastic and plastic components of the total strain amplitudes are also presented.

ε[-]	σ_a [MPa]	ε_e [-]	ε_p [-]
0.0019	654.2	0.0020	-0.0001
0.0030	740.9	0.0023	0.0007
0.0040	779.7	0.0024	0.0017
0.0051	813.9	0.0025	0.0026
0.0061	836.6	0.0026	0.0035
0.0071	852.5	0.0026	0.0044
0.0081	869.8	0.0027	0.0054
0.0090	876	0.0027	0.0064
0.0101	882.5	0.0027	0.0074

The data at 0.2% strain amplitude was not used for the computations according to [2], [13], where it is suggested that strains lower than 0.0005 [mm/mm] should be neglected to avoid calculation errors. On the other hand, the Young´s modulus for the CSS was estimated as the slope of the line between the origin and the peak point at 0.2% strain amplitude in the graph. To facilitate the calculations it was assumed that Young´s modulus was constant for each strain loop which, in essence, seems to be true and just some small variations are seen at higher strains.

As it was mentioned in section 2.3.1, the stress vs. plastic strain amplitude follows a straight line when plotted in a logarithmic scale.

The estimators of the curve A and B and the variance are, respectively:

$A = 3.11$ $B = 0.08$ $\sigma = 0.002$

Hence, the cyclic strength coefficient and the cyclic strain hardening exponent are, respectively:

$K' = 1314\text{MPa}$ $n' = 0.08$

In the case of the estimation of the tensile parameters some assumptions had to be made. Since the instantaneous test section area was not able to measure, the engineering stresses and strains were used for the computations. Even when this is not corresponding to literature, it was thought to be a reasonable assumption since the final area at fracture was measured and it was seen that it did not decrease much. Again, those strains lower than 0.0005 [mm/mm] were not taken into account to do the computations. The estimators of the best fit line are:

$A = 3.00$ $B = 0.07$ $\sigma = 0.007$

then,

$K = 1008\text{MPa}$ $n_m = 0.07$

Despite there is not a big difference between the cyclic and monotonic strain hardening exponents, it may be concluded that D176 will harden when undergoing cyclic loading. This is also seen in figure 4.32, where the monotonic curve falls below the cyclic stress-strain curve. This explains why this material yields at a higher stress under cyclic loading than under monotonic loading.

Chapter 5: Conclusions

The *S-N* curves for the alloys show that Densimet 176 has higher fatigue strength than Inermet 180. Even though the exact endurance limits for the alloys were not obtained, they are estimated to be about 45% and 33% of the UTS for the former and latter, respectively.

Tungsten content affects the fatigue behavior of these alloys. In this sense, the lower the tungsten content, the better the fatigue properties which explains why D176, having 92.5wt% of tungsten, has a higher fatigue strength than IT180 with 95wt% of tungsten.

Porosity was a common defect present in both alloys. However its effect has been more detrimental in the case of IT180 who presented bigger pores, with very irregular shapes and in a large number, acting as stress concentrations and zones of crack initiation. The scatter in the fatigue data for this alloy is higher than that of D176 and might be related to this fact.

The use of stress-controlled testing for the estimation of the *S-N* curve is fairly valid since all the specimens endured more than 10^4 cycles before failing, proving that the experiments were in the high cycle fatigue regime, where this type of test is suitable.

Since the *S-N* relationship was approximated by a straight line within the interval of stresses tested, and because the actual fatigue distribution is unknown, the results obtained should not be extrapolated to other stress levels and are only valid within the test interval.

Surface roughness has a detrimental effect on crack initiation in a material under cyclic loading. Grinding and polishing to reduce lines on the surface of the specimens suppressed this effect, gaining the reproducibility of the fatigue results.

The stress concentration associated with the blend radius of the tested specimens may have caused that some of the specimens broke near the grips. For more accurate results, testing samples with the same shapes as the target will have when operating in the spallation device would be preferred.

The principal fracture mechanism under fatigue loading observed in D176 was tungsten grain cleavage similar to what also has been observed for ductile WHAs under tensile loading conditions. In the case of IT180, failure by separation of W-W interfaces was predominant which reduces the load that can be carried by the grains and, thereby, its fatigue strength.

The estimation of the cyclic stress-strain curve showed that both alloys harden under cyclic loading compared to their response under monotonic tensile loading. The cyclic strain hardening exponent and the cyclic yield strength of D176 were determined and are higher than the monotonic strain hardening exponent and yield strength.

IT180 is very sensitive to misalignment during the strain-controlled tests due to its brittleness and broke at low strain amplitude levels, and thus it was not possible to find the cyclic parameters n' and σ'_y for this alloy.

References

[1] European Spallation Source. Inside Materials: Seeing with Neutron Eyes. http://ess-scandinavia.eu/documents/ess_neutron_eyes.pdf

[2] European Spallation Source ESS AB. Interim Report For First Quarter 2011. https://maiserxx.esss.lu.se/press/documents/Q1_2011_ENG_FINAL.pdf

[3] C. Vettier, C. Carlile, P. Carlsson. Progress for the European spallation source in Scandinavia. Nuclear Instruments and Methods in Physics Research Section A: Accelerators, Spectrometers, Detectors and Associated Equipment, Volume 600, Issue 1, 21 February 2009, Pages 8-9.

[4] American Society of Testing and Materials. Standard Practice for Statistical Analysis of Linear or Linearized Stress-Life (S-N) and Strain-life (e-N) Fatigue Data. E739.1991 (reapproved 1998).

[5] S. Lin, Y. Lee, M. Lu. Evaluation of the staircase and the accelerated test methods for fatigue limit distributions. International Journal of Fatigue. Vol 23, Issue 1, January 2001, Pages 75-83

[6] ASM International. ASM Handbook. Formerly Ninth Edition, Metals Handbook. Vol 7: Powder Metallurgy. United States of America. 1984.

[7] ASM International. ASM Handbook. Formerly Tenth Edition, Metals Handbook. Vol 2: Properties and Selection: Nonferrous Alloys and Special-Purpose Materials. United States of America. 1990.

[8] D.V. Edmonds. Structure/property relationships in sintered heavy alloys. International Journal of Refractory Metals and Hard Materials.Vol 10, Issue 1, 1991, Pages 15-26.

[9] J. Dasa, G. Appa Raoa, S.K. Pabib. Microstructure and mechanical properties of tungsten heavy alloys. Materials Science and Engineering: A.Vol 527, Issues 29-30, 2010, Pages 7841-7847.

[10] J. Fenollosa Coral, J.Bigordà Peiró. La fatiga dels elements mechanics. Fenollosa Publication: 01/01/1996 Editorial: Edicions de la UPC. Temes denginyeria mecànica, Catalan, 62 pages.

[11] S. Suresh. Fatigue of materials. 2nd ed. New York: Cambridge University Press, 1998.

[12] P. Wirsching. Satistical Summaries of Fatigue Data for Design Purposes. NASA contractor report 3697

[13] Y.L. Lee, J. Pan, R. B. Hathaway, M. E. Barkey. Fatigue testing and analysis. 200 Wheeler Road, Burlington, MA 01803, USA; Linacre House, Jordan Hill, Oxford OX2 8DP, UK. Elsevier Butterworth Heinemann, 2005.

[14] American Society of Testing and Materials. Standard Practice for Presentation of Constant Amplitude Fatigue Test Results for Metallic Materials. E468. 1990 (reapproved 1998).

[15] American Society of Testing and Materials. Standard Terminology Relating to Methods of Mechanical Testing. E6. 1999.

[16] C.M. Sonsino. Fatigue design for powder metallurgy. Metal Powder Report. Vol 45, Issue 11, November 1990, Pages 754-764.

[17] A. Jones, R. C. Hudd. Cyclic stress-strain curves generated from random cyclic strain amplitude tests. International Journal of Fatigue, Vol 21, Issue 6, July 1999, Pages 521-530.

[18]American Society of Testing and Materials. Standard Practice for Strain-Controlled Fatigue Testing. E606. 1992 (reapproved 1998).

[19] J. Polák, M. Hájek. Cyclic stress-strain curve evaluation using incremental step test procedure. International Journal of Fatigue. Vol 13, Issue 3, May 1991, Pages 216-222.

[20] J. Polák, M. Klesnil, P. Lukáš. On the cyclic stress-strain curve evaluation in low cycle fatigue.Materials Science and Engineering. Vol 28, Issue 1, April 1977, Pages 109-117.

[21] S.Danesh Sundara Raman, K.A. Padmanabhan. Determination of the room-temperature cyclic stress—strain curve of AISI 304LN austenitic stainless steel by two different methods. International Journal of Fatigue, Vol 14, Issue 5, September 1992, Pages 295-304.

[22] R.C. Hibbeler. Mechanics of materials. 2nd ed. Singapore: Prentice Hall Pearson Education South Asia Pte Ltd. 2005.

[23] American Society of Testing and Materials. Standard Practice for Conducting Force Controlled Constant Amplitude Axial Fatigue Tests of Metallic Materials. E466. 1996.

[24] American Society of Testing and Materials. Standard Test Methods for

Tension Testing of Metallic Materials. E8. 2000.

[25] D. Hull. Fractography: observing, measuring, and interpreting fracture surface topography. Cambridge University Press. United Kingdom. 1999

[26] N. Chawla, X. Deng. Microstructure and mechanical behavior of porous sintered steels.Materials Science and Engineering A. Vol 390, Issues 1-2, 15 January 2005, Pages 98-112

[27] N. Chawlaa, T.F. Murphya, K.S. Narasimhana, M. Koopmanb and K.K. Chawlab.

Axial fatigue behavior of binder-treated versus diffusion alloyed powder metallurgy steels. Materials Science and Engineering: A.Vol 308, Issues 1-2, 30 June 2001, Pages 180-188

[28] K.M. Ostolaza Zamora, J.Gil Sevillano, M. Fuentes Pérez. Fracture toughness of W heavy metal alloys. Materials Science and Engineering: A.Vol 157, Issue 2, 1 October 1992, Pages 151-160.

[29] R. L. Woodward, R.G. O´Donnell. Tensile rupture of tungsten alloys by cascade of crack nucleation events.Journal of materials science. Vol 35, 2000, Pages 4067-4072.

Appendix A Statistical analysis of linearized Stress-Life curve fatigue data

Fatigue Data from the tests:

	Stress levels:	Cycles to failure:

Inermet 180:

$$S_I := \begin{pmatrix} 300 \\ 300 \\ 250 \\ 250 \\ 225 \\ 225 \\ 210 \\ 210 \\ 210 \end{pmatrix} \qquad N_I := \begin{pmatrix} 33831 \\ 40177 \\ 329748 \\ 139854 \\ 424545 \\ 336042 \\ 312378 \\ 2.00E+06 \\ 1626921 \end{pmatrix}$$

Densimet 176

$$S_D := \begin{pmatrix} 550 \\ 550 \\ 500 \\ 500 \\ 450 \\ 450 \end{pmatrix} \qquad N_D := \begin{pmatrix} 258788 \\ 213838 \\ 629575 \\ 958423 \\ 885444 \\ 1468220 \end{pmatrix}$$

*The subscripts "I" and "D" refer to Inermet 180 and Densimet 176, respectively.

Now, expressing the data on logarithmic scale:

$$Y(N) := \text{for } i \in 0..\text{rows}(N) - 1 \\ \left| \begin{matrix} Y_i \leftarrow \log(N_i) \\ Y \end{matrix} \right. \qquad X(S) := \text{for } i \in 0..\text{rows}(S) - 1 \\ \left| \begin{matrix} X_i \leftarrow \log(S_i) \\ X \end{matrix} \right.$$

New variables definition:

Life of IT180: $\qquad Y_I := Y(N_I)$

Stress of IT180: $\qquad X_I := X(S_I)$

Life of D176: $\qquad Y_D := Y(N_D)$

Stress of D176: $\qquad X_D := X(S_D)$

The average of the stress and the fatigue life taken from Eqs 2.15 and 2.16, respectively :

$$Y_I := \frac{\sum Y_I}{\text{rows}(Y_I)} = 5.44 \qquad\qquad X_I := \frac{\sum X_I}{\text{rows}(X_I)} = 2.38$$

$$Y_D := \frac{\sum Y_D}{\text{rows}(Y_D)} = 5.773 \qquad\qquad X_D := \frac{\sum X_D}{\text{rows}(X_D)} = 2.698$$

The maximum likelihood estimators are calculated as follows:

The nominator of Eq. 2.14 is:

$$\text{Bup}(X,Y,X,Y) := \text{for } i \in 0..\text{rows}(X) - 1$$
$$\left| \begin{array}{l} \text{Bup}_i \leftarrow (X_i - X)(Y_i - Y) \\ \text{Bup} \end{array} \right.$$

The denominator from Eq 2.14 is:

$$\text{Bdown}(X,Y,X) := \text{for } i \in 0..\text{rows}(X) - 1$$
$$\left| \begin{array}{l} \text{Bdown}_i \leftarrow (X_i - X)^2 \\ \text{Bdown} \end{array} \right.$$

$$\text{Bup}_D := \text{Bup}(X_D, Y_D, X_D, Y_D) \qquad \text{Bdown}_D := \text{Bdown}(X_D, Y_D, X_D)$$

$$\text{Bup}_I := \text{Bup}(X_I, Y_I, X_I, Y_I) \qquad \text{Bdown}_I := \text{Bdown}(X_I, Y_I, X_I)$$

The estimators of IT180 are:

$$\boxed{B_I := \frac{\sum \text{Bup}_I}{\sum \text{Bdown}_I} = -8.967} \qquad \boxed{A_I := Y_I - B_I \cdot X_I = 26.783}$$

$$\boxed{B_D := \frac{\sum \text{Bup}_D}{\sum \text{Bdown}_D} = -7.791} \qquad \boxed{A_D := Y_D - B_D \cdot X_D = 26.7902}$$

Expected fatigue life for each stress level according to the estimators

$$y_I := A_I + B_I \cdot X_I$$

$$y_D := A_D + B_D \cdot X_D$$

The variance is:

IT180:

$$\text{Square}\sigma_I := \frac{\sum (Y_I - y_I)^2}{\text{rows}(Y_I) - 2} = 0.072 \qquad \sigma_I := \sqrt{\text{Square}\sigma_I} = 0.268$$

D176:

$$\text{Square}\sigma_D := \frac{\sum (Y_D - y_D)^2}{\text{rows}(Y_D) - 2} = 0.023 \qquad \sigma_D := \sqrt{\text{Square}\sigma_D} = 0.153$$

The fatigue strength exponents are:

$$\boxed{b_I := \frac{1}{B_I} = -0.112}$$

$$\boxed{b_D := \frac{1}{B_D} = -0.128}$$

The fatigue strength coefficients are:

$$\boxed{Sf_I := 10^{\frac{-A_I}{B_I}} \cdot \left(\frac{1}{2}\right)^{b_I} = 1.048 \times 10^3}$$

$$\boxed{Sf_D := 10^{\frac{-A_D}{B_D}} \cdot \left(\frac{1}{2}\right)^{b_D} = 2.999818 \times 10^3}$$

The term "1/2" is added because Basquin´s equation is expressed in number of

reversals to failure instead of cycles to failure which is the measured variable.

The median curves in a Basquin´s equation fashion for each alloy are expressed as:

$$Sa_I(x) := Sf_I \cdot (2x)^{b_I}$$

$$Sa_D(x) := Sf_D \cdot (2x)^{b_D}$$

Estimation of the design curve:

Variables definition:

$$K_R := \text{qnorm}(0.90, 0, 1) = 1.282 \qquad\qquad K_C := \text{qnorm}(0.95, 0, 1) = 1.645$$

$$f_I := \text{rows}(Y_I) - 2 \qquad\qquad f_D := \text{rows}(Y_D) - 2$$

$$a_I := \frac{1.85}{\text{rows}(Y_I)} \qquad\qquad a_D := \frac{1.85}{\text{rows}(Y_D)} = 0.308$$

Empirical coefficients for K_{OWEN} with 95% confidence level

$$b1 := 0.9968 \qquad b2 := 0.1596 \qquad b3 := 0.60 \qquad b4 := -2.636$$

Note that b1, b2, b3 and b4 are the same for both alloys. The rest of the constants are:

$$c1_I := 1 + \frac{3}{4 \cdot (f_I - 1.042)} = 1.126 \qquad\qquad c1_D := 1 + \frac{3}{4 \cdot (f_D - 1.042)} = 1.254$$

$$c2_I := \frac{f_I}{f_I - 2} = 1.4 \qquad\qquad c2_D := \frac{f_D}{f_D - 2} = 2$$

$$c3_I := c2_I - c1_I{}^2 = 0.132 \qquad\qquad c3_D := c2_D - c1_D{}^2 = 0.429$$

$$K_I := c1_I \cdot K_R + K_C \cdot \sqrt{c3_I \cdot K_R{}^2 + c2_I \cdot a_I} = 2.612$$

$$K_D := c1_D \cdot K_R + K_C \cdot \sqrt{c3_D \cdot K_R{}^2 + c2_D \cdot a_D} = 3.497$$

$$\text{Rowen}_I := b1 + \frac{b2}{f_I{}^{b3}} + b4 \cdot e^{-f_I} \qquad\qquad \text{Rowen}_D := b1 + \frac{b2}{f_D{}^{b3}} + b4 \cdot e^{-f_D}$$

$$\text{Kowen}_I := K_I \cdot \text{Rowen}_I = 2.727 \qquad\qquad \text{Kowen}_D := K_D \cdot \text{Rowen}_D = 3.56$$

The fatigue coefficient for the design curve of each alloy is:

$$S'_I := 10^{\frac{A_I - Kowen_I \cdot \sigma_I}{-B_I}} \cdot \left(\frac{1}{2}\right)^{b_I} \qquad S'_D := 10^{\frac{A_D - Kowen_D \cdot \sigma_D}{-B_D}} \cdot \left(\frac{1}{2}\right)^{b_D}$$

$$\boxed{S'_I = 868.318} \qquad \boxed{S'_D = 2.553 \times 10^3}$$

Appendix B Empirical coefficients for K_{OWEN}

Following are tabulated the empirical coefficients to estimate K_{OWEN} extracted from reference [13] (Page 116).

Confidence Level (C)	b_1	b_2	b_3	b_4
0.95	0.9968	0.1596	0.60	-2.636
0.90	1.0030	-6.0160	3.00	1.099
0.85	1.0010	-0.7212	1.50	-1.486
0.80	1.0010	-0.6370	1.25	-1.554

	c_1	c_2	c_3
$f < 2$	1	1	$\dfrac{1}{2f}$
$f \geq 2$	$1 + \dfrac{3}{4(f - 1.042)}$	$\dfrac{f}{f - 2}$	$c_2 - c_1{}^2$

Appendix C Sample pictures after fracture

In this chapter, pictures of all the samples after testing are shown, and it is clearly seen that almost all of them broke, but mainly at the ends of testing section, as mentioned in the report.

IT180 Specimen #1

IT180 Specimen #2

IT180 Specimen #3

IT180 Specimen #4

IT180 Specimen #5

IT180 Specimen #6

IT180 Specimen #7

IT180 Specimen #8

IT180 Specimen #9

IT180 Specimen #10

IT180 Specimen #11

IT180 Specimen #12

IT180 Specimen #13

IT180 Specimen #14

IT180 Specimen #15

IT180 Specimen #16

IT180 Specimen #17

D176 Specimen #1

D176 Specimen #2

D176 Specimen #3

D176 Specimen #4

D176 Specimen #5

D176 Specimen #6

D176 Specimen #7

D176 Specimen #8

D176 Specimen #9

D176 Specimen #10